Royal Holloway
and Bedford New College

Department of Physics

University of London

First Year Report: Cavity Optomechanics with Nanofluidic Geometries

Author:
Sebastian Spence
Peap011@live.rhul.ac.uk

Supervisor:
Dr. Rojas

June 18, 2018

Contents

Chapter 1:

Cavity Quantum Optomechanics

1.1 Introduction

This report will summarise the first year of studies into Cavity Optomechanics with Nanofluidic Geometries. It will include introductions to microwave cavities and cavity optomechanics. Along with methodology for the creation of a first generation of phononic lattice defect chips and initial choice of two re-entrant cavities.

Optomechanics is the field of physics concerned with the interaction between electromagnetic radiation and mechanical systems. Classically this is via radiation pressure, postulated all the way back in 1619 by Kepler's observation of comet dust trails pointing away from the sun[1]. In more recent times the field has developed beyond the classical regime and expanded to include: laser cooling[2], interferometry for gravitational waves[3], quantum information[4], and many other diverse areas. Cavity optomechanics focuses on interactions between photons contained within optical resonators (cavities) and mechanical systems. These studies form the bulk of optomechanics, though experiments in absence of cavities are under way in fields such as photonic circuits and photonic crystal fibres[5][6].

This project is concerned with the quantum end of optomechanics, categorised by low energy regimes and nano-scale geometries, with much overlap to the study of nano-electro-mechanical systems (NEMS). The intent is to explore photon-phonon coupling, the particle representations of electromagnetic radiation and mechanical vibrations, a difficult to access but interesting quantum regime. This will be achieved by coupling superconducting microwave cavities to nano-scale superfluid acoustic resonators, both having the advantage of extremely high quality factors. Superfluid Helium-4 (^{4}He) at low mK temperatures, confined within pseudo 2D phononic lattices, will be used to form the acoustic resonator. Taking advantage of superfluid ^{4}He's exceptionally low dissipation to create mechanical systems with high sensitivity and phonon lifetime. This will be used to investigate the effects of electrostrictive optomechanical coupling and acoustic non-linearities to explore phonon-photon interactions. The hopes of this project is to understand and develop the techniques of combined nanofluidic and optomechanical systems.

1.2 Electromagnetic Cavity Modes

This section will cover the electromagnetic modes of cylindrical and rectangular microwave cavities. Though re-entrant cavity modes used later in this report differ from hollow cavity modes, they are still useful as a base model for understanding coupling and losses in re-entrant cavities. These models will be compared to a lumped element circuit approach in Chapter 3.

1.2.1 Rectangular TEM modes:

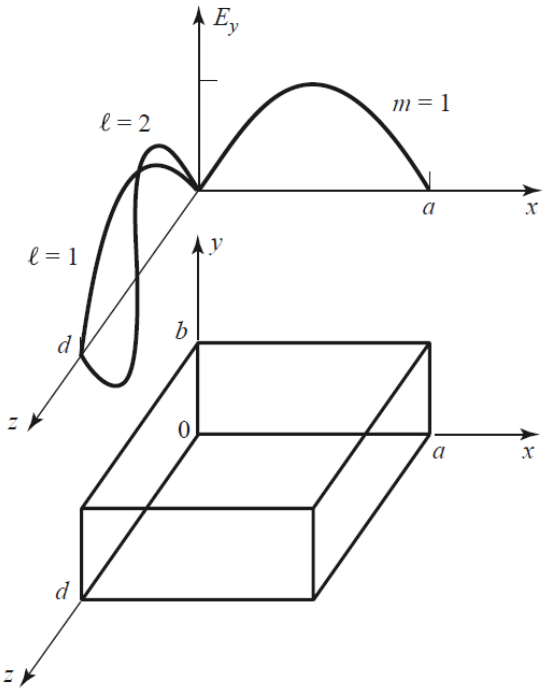

Figure 1.1: A rectangular cavity resonator with the electric field magnitude variations for the TE_{101} and TE_{102} resonant modes shown. Extracted from [7].

The theory of which is covered in Pozar chapter 6.3. Transverse Electro-Magnetic (TEM) modes of wave guides are split into: Transverse Electric (TE) modes, where there is no electric field in the direction of propagation; and transverse magnetic (TM) modes, where there is no magnetic field in the direction of propagation. The resonant TEM frequencies of a rectangular cavity are calculated by taking a rectangular waveguide shorted at both ends. The mode-shape of the electric field is a standing wave with nodes at the cavity edges (Figure 1.1). The frequencies f_{mnl} of the resonant TE_{mnl} modes are given by the equation [7].

$$f_{mnl} = \frac{ck_{mnl}}{2\pi\sqrt{\mu_r \epsilon_r}} \tag{1.1}$$

The numbers mnl refer to the number of half wavelengths of the TE standing wave in the xyz planes of the cavity. c is the speed of light in the medium, then μ_r and ϵ_r are the relative permeability and permittivity respectively. k_{mnl} the wave number of the mode is given by:

$$k_{mnl} = \sqrt{\left(\frac{m\pi}{a}\right)^2 + \left(\frac{n\pi}{b}\right)^2 + \left(\frac{l\pi}{d}\right)^2} \tag{1.2}$$

Where a, b, d are the dimensions of the sides of planes m, n, l respectively. The TM_{mnl} modes are of the same frequency as their TE_{mnl} counterparts, so an additional equation is not required, and no degeneracy is present. Note on resonance an equal proportion of energy is stored in the electric and magnetic fields, this is true for all cavities and is analogous to energy storage in an LC circuit resonator.

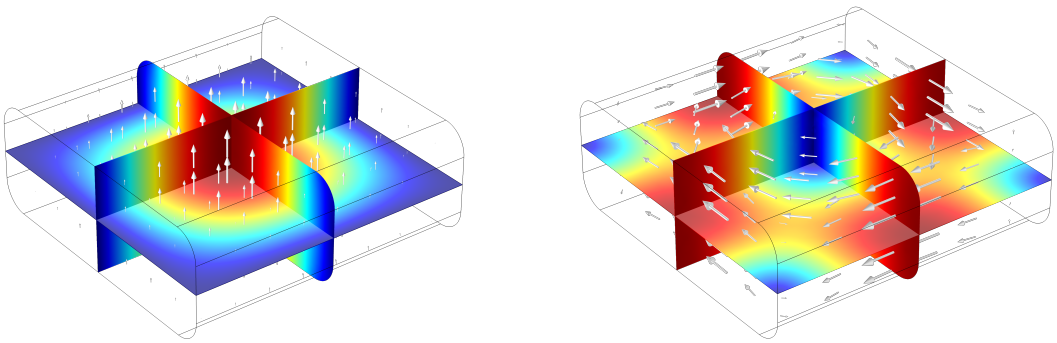

Figure 1.2: Left: Electric field norm of a rectangular cavity TE_{110} mode. Right: Magnetic field norm of a rectangular cavity TM_{110} mode. Arrows show field direction and strength

Figure 1.2 shows the TE_{110} and TM_{110} modes of a rectangular cavity, with arrows showing field direction. This is the fundamental (lowest f_0) mode of a cavity of this shape. The filleted corners are due to fabrication, as this was the cavity size used during a research trip to UofA[1] (16mm×16mm×10mm and $f_0 \approx 13$ GHz). This cavity and mode shape are suitable for SMA pin coupling from the top or bottom face, in line with electric field; or with a loop cutting the magnetic field, or acting as a magnetic dipole within a port for weaker coupling.

[1]Davis Lab, University of Alberta, *Feb 2017*

1.2.2 Cylindrical TE/TM modes:

The theory of which is covered in Pozar chapter 6.4. Similarly to the rectangular case these modes are found by shorting a cylindrical wave guide at either end, giving the same standing wave form in the $\hat{z}$ direction, Figure 1.3. The TM and TE resonant modes are separate, which can lead to degeneracies or splitting based on cavity dimensions. Both modes are specified by the indices n, m, l which give the number of nodes in the magnetic, or electric, field in directions ϕ, ρ, z respectively (not in the order of cylindrical coordinates[7]).

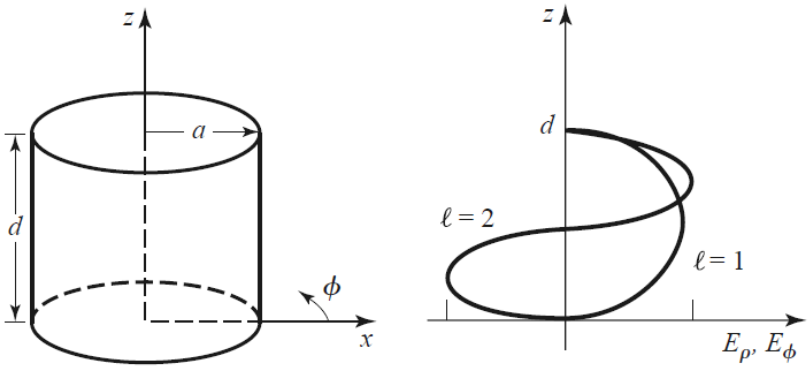

Figure 1.3: A cylindrical cavity resonator, and the electric field variations for $l = 1$ and $l = 2$ resonant modes. Extracted from [7].

The frequency of the TE_{nml} modes is given by:

$$f_{mnl} = \frac{c}{2\pi\sqrt{\mu_r \epsilon_r}} \sqrt{\left(\frac{p'_{nm}}{a}\right)^2 + \left(\frac{l\pi}{d}\right)^2} \tag{1.3}$$

Where p'_{nm} is the m-th zero of the derivative of the n-th Bessel function. And the frequency of the TM_{nml} modes is given by:

$$f_{mnl} = \frac{c}{2\pi\sqrt{\mu_r \epsilon_r}} \sqrt{\left(\frac{p_{nm}}{a}\right)^2 + \left(\frac{l\pi}{d}\right)^2} \tag{1.4}$$

Where p_{nm} is the m-th zero of the n-th Bessel function.

Figure 1.4 shows the TE_{011} mode, by controlling cavity dimensions this can be reduced to the sixth lowest frequency mode [7]. The fundamental TM_{010} mode shape is very similar to the TEM_{110} of the rectangular cavity, however the TE_{011} mode has the highest potential Q factor. This is due to minimum electric field and low magntic field at all cavity walls minimising dielectric and conductor losses respectively. Additionally

seams located at minima for both fields minimise associacted losses. These effects are discussed further in[8] and [9]. SMA pin coupling to this mode is more difficult than the TM_{010} mode, due to the lack of electric field at the surfaces, although may be possible from the side with a pin in the direction of the electric field. Magnetic loop coupling is of similar complexity to the rectangular case.

Figure 1.4: Left: Electric field norm of a cylindrical cavity TE_{011} mode. Right: Magnetic field norm of a cylindrical cavity TE_{011} mode. Arrows show field direction and strength

1.3 Optomechanical Coupling

This section will cover the theory leading to the cavity optomechanical coupling constant g_0, expressed in terms of variables calculable by finite element modelling (FEM). The general linearised cavity optomechanical Hamiltonian is [10]:

$$H = \hbar\omega_c a^\dagger a + \hbar\Omega_m b^\dagger b + \hbar g_0 a^\dagger a(b^\dagger + b) \tag{1.5}$$

Where $\hbar$ is the reduced Planck constant, ω_c is the cavity resonant frequency, $a^\dagger a$ the photon creation and annihilation operators, Ω_m the mechanical resonant frequency, $b^\dagger b$ the phonon creation and annihilation operators, and g_0 is the optomechanical coupling factor, the optical resonant frequency shift due to the mechanical oscillator in its ground state. $g_0 = Gx_{zpf}$ where $G = -\partial\omega_c/\partial x$ and x_{zpf} is the mechanical zero-point displacement. g_0 is also called the single photon coupling rate, which is analogues to the average frequency shift of a photon on resonance entering an optically empty cavity per phonon present in the acoustic mode.

Considering the definition of $g_0 = \delta\omega_c$, with $\delta\omega_c$ being the cavity resonance shift due to the zero-point motion of the mechanical resonator. The mechanical resonator is formed by oscillating pressure waves within the microwave cavity environment, either in a confined nanofluidic or filled cavity environment. These pressure waves cause density

fluctuations, which cause fluctuations in the permeability and permittivity of the cavity, in turn changing the energy and therefore resonant frequency of the optical mode. So relating $\delta\omega_c$ to $\delta\epsilon$ and $\delta\mu$, then finally to $\delta\rho$ will give an equation for the cavity optomechanical coupling g_0. Note these are all changes due to zero-point motion. From Pozar section 6.7 [7] the fractional change in resonant frequency due to material fluctuations:

$$\frac{\delta\omega_c}{\omega_c} \simeq -\frac{\int_V \delta\epsilon|\vec{E_0}(\vec{r})|^2 + \delta\mu|\vec{H_0}(\vec{r})|^2 \, d^3\vec{r}}{\int_V \epsilon|\vec{E_0}(\vec{r})|^2 + \mu|\vec{H_0}(\vec{r})|^2 \, d^3\vec{r}} \tag{1.6}$$

Where $\vec{E_0}$ and $\vec{H_0}$ are the unperturbed fields, $\int_V$ is over the cavity volume, and $\delta\epsilon$ & $\delta\mu$ are respectively the change in permittivity and permeability, due to zero-point motion. Using the knowledge that on resonance energy in the fields are equal, that $\delta\mu \ll \delta\epsilon$ due to an almost zero magnetic susceptibility in ^{4}He (true for non-magnetic materials), and cancelling ϵ_0 factors, simplifies this equation to:

$$\delta\omega_c \simeq -\frac{\omega_c}{2\epsilon_r}\frac{\int_V \delta\epsilon_r|\vec{E_0}(\vec{r})|^2 \, d^3\vec{r}}{\int_V |\vec{E_0}(\vec{r})|^2 \, d^3\vec{r}} \tag{1.7}$$

With $\delta\epsilon_r$ being the change in relative permittivity due to zero-point motion. To relate permittivity to density the Clausius-Mosotti Equation[11] is used:

$$\frac{\epsilon_r - 1}{\epsilon_r - 2} = \frac{4\pi\rho\alpha_M}{3M} \tag{1.8}$$

Where ρ is the density, α_M is the molar polarisation, and M the molar mass. Differentiating with respect to ρ and relating molar polarisation and mass to ϵ_r via the electric susceptibility gives:

$$\frac{\partial\epsilon_r}{\partial\rho} = \frac{(\epsilon_r + 2)(\epsilon_r - 1)}{3\rho} \tag{1.9}$$

Using this to write $\delta\epsilon_r$ in terms of $\delta\rho$:

$$\delta\epsilon_r = \frac{(\epsilon_r + 2)(\epsilon_r - 1)}{3}\frac{\delta\rho}{\rho} \tag{1.10}$$

Where both $\delta\epsilon_r$ and $\delta\rho$ are changes due to zero-point motion of the mechanical resonator. $\delta\epsilon_r$ in (Eq(1.7)) will have a dependence on $\vec{r}$, therefore expressing $\delta\rho$ in terms of the a mode shape function $f(\vec{r})$ [12]:

$$\delta\rho(\vec{r}) \equiv \delta\rho_{zpf} f(\vec{r}) \tag{1.11}$$

Where $\delta\rho_{zpf}$ is the maximum amplitude of the zero-point density fluctuation due to the superfluid helium resonant mode and $f(\vec{r})$ is the mode shape function. $f(\vec{r})$ is normalised

such that $|f(\vec{r})| \leq 1$, this normalisation is valid provided ρ_{zpf} is the physical density fluctuations [12]. Substituting Eq(1.11) and Eq(1.10) into Eq(1.7) gives:

$$\delta\omega_c \simeq -\omega_c \frac{(\epsilon_r+2)(\epsilon_r-1)}{6\epsilon_r}\left(\frac{\delta\rho_{zpf}}{\rho}\right)\frac{\int_V f(\vec{r})|\vec{E_0}(\vec{r})|^2\ d^3\vec{r}}{\int_V |\vec{E_0}(\vec{r})|^2\ d^3\vec{r}} \tag{1.12}$$

To write this equation in terms of factors calculable via finite element modelling (FEM) $\delta\rho_{zpf}$ must be rewritten, this is achieved via the energy of the mode and definition of compressibility. On resonance the kinetic and potential energy of a mechanical mode are equal, giving the total energy E:

$$E = \int_V e_{PE}(\vec{r}) + e_{KE}(\vec{r})\ d^3\vec{r} \ = \ 2\int_V e_{PE}(\vec{r})\ d^3\vec{r} \tag{1.13}$$

With $e_{PE}(\vec{r})$ and $e_{KE}(\vec{r})$ the potential and kinetic energies respectively. By definition the energy of the ground state or zero point energy is:

$$\begin{aligned} E &= \frac{\hbar\Omega_m}{2} \\ &= 2\int_V e_{PE}(\vec{r})\ d^3\vec{r} \end{aligned} \tag{1.14}$$

Where this has been related to Eq(1.13) in the second line. Writing the acoustic potential energy in terms of pressure[13]:

$$e_{PE}(\vec{r}) = \frac{1}{2\rho c^2}(\delta P(\vec{r}))^2 \tag{1.15}$$

Where c is the speed of sound within the material and $\delta P(\vec{r})$ is the pressure differential. Pressure can be related to density via the definition for compressibility β:

$$\beta = -\frac{1}{V}\frac{\partial V}{\partial P} = \frac{1}{\rho}\frac{\partial \rho}{\partial P} \tag{1.16}$$

Where V is the volume, and the differential of $\rho = M/V$ is used in the second equality. In the isentropic case:

$$\beta_S = \frac{1}{\rho c^2} \tag{1.17}$$

Where β_S is the compressibility at constant entropy. Using this and Eq(1.16) to rewrite Eq(1.15):

$$e_{PE}(\vec{r}) = \frac{1}{2\rho c^2}\left(\frac{\delta\rho(\vec{r})}{\rho}\right)^2 \tag{1.18}$$

Substituting this into Eq(1.14) and rewriting $\delta\rho(\vec{r})$ using Eq(1.11) gives:

$$\frac{\hbar\Omega_m}{2} = \frac{1}{\rho c^2}\left(\frac{\delta\rho_{zpf}}{\rho}\right)^2 \int_V f(\vec{r})^2 d^3\vec{r} \tag{1.19}$$

Rearranging this to be in terms of $\delta\rho_{zpf}/\rho$:

$$\frac{\delta\rho_{zpf}}{\rho} = \sqrt{\frac{\hbar\Omega_m}{2\rho c^2 \int_V f(\vec{r})^2 d^3\vec{r}}} \tag{1.20}$$

Finally substituting this into Eq(1.12) gives the optomechanical coupling constant as:

$$g_0 = -\omega_c \frac{(\epsilon_r+2)(\epsilon_r-1)}{6\epsilon_r}\sqrt{\frac{\hbar\Omega_m}{2\rho_h c_h^2 \int_V f(\vec{r})^2 d^3\vec{r}}}\frac{\int_V f(\vec{r})|\vec{E_0}(\vec{r})|^2 d^3\vec{r}}{\int_V |\vec{E_0}(\vec{r})|^2 d^3\vec{r}} \tag{1.21}$$

To summarise: ρ_h and c_h are the bulk density and speed of sound of the medium filling the cavity (^{4}He), $f(\vec{r})$ is the acoustic modeshape function normalised as $|f(\vec{r})| \leq 1$ and $\vec{E_0}(\vec{r})$ is the electric field magnitude vector of the resoant cavity mode coupling to the mechanical mode. $V_{eff} = \int_V f(\vec{r})^2 d^3\vec{r}$ represents the effective volume of the acoustic resonant mode, which translates directly to an effective mass. $\int_V f(\vec{r})|\vec{E_0}(\vec{r})|^2 d^3\vec{r}$ represents an overlap integral between the electronic and acoustic modes, normalised by the denominator. Eq(1.21) can also be written in terms of pressure using $g_0 = \partial\omega_c/\partial P \cdot \delta P_{zpf}$ as [14]:

$$g_0 = -\omega_c \beta \delta P_{zpf} \frac{(\epsilon_r+2)(\epsilon_r-1)}{6\epsilon_r}\frac{\int_V f(\vec{r})|\vec{E_0}(\vec{r})|^2 d^3\vec{r}}{\int_V |\vec{E_0}(\vec{r})|^2 d^3\vec{r}} \tag{1.22}$$

Where δP_{zpf} is the maximum pressure difference due to zero point motion of the mode, which when expanded causes the above equation to become Eq(1.21). Using FEM to separately simulate the acoustic and electromagnetic modes, all the values in Eq(1.21) can be calculated. This becomes a powerful tool in designing optomechanical systems. As g_0 is a measure of coupling strength, this allows comparison not only between differing geometries, but also entirely different optomechanical schemes. When moving from simulation to experimental testing it will be important to determine the accuracy of simulated g_0 factors.

Chapter 2:

Nanofluidic Geometry & Cavity Optomechanics

2.1 Nanofluidic Geometry

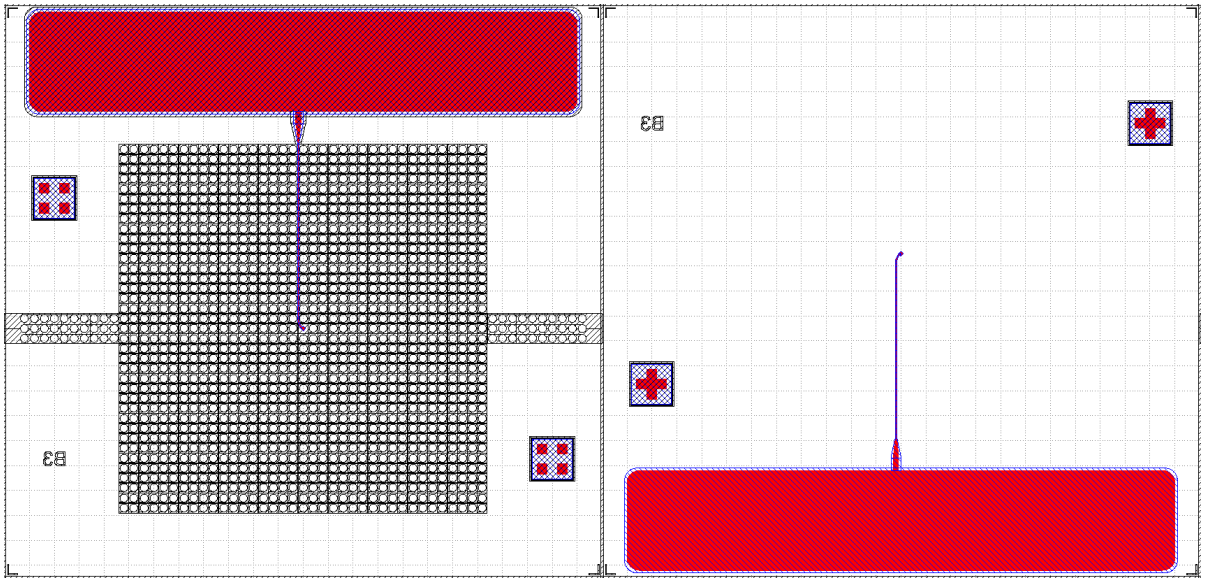

Figure 2.1: The top and bottom B3 chip geometries rendered in KLayout for fabrication. The black regions represent the first glass etch, the blue the second glass etch and the red the deposited Aluminium. The large red regions top and bottom are the antenna/regions for galvanic bonding, with thin wires leading to the central capacitor plates. These antenna and wires are sunk within the second blue etch, such that they lay flat with the first black etch. The circular pillars of the acoustic lattice can be seen within the black etch.

The proposed geometry for this project is of a borosilicate/quartz chip confining a near-2D nanofluidic geometry within itself, to be placed within a microwave cavity. The chip is formed of a top and bottom piece directly bonded together, confining the

2D nanofluidic environment between the two pieces. The optical mode of the microwave cavity is coupled to the acoustic mode of the chip via either galvanic coupling to the cavity walls or by large on chip antenna, both of which then have thin μm thick on chip wires leading to a central capacitive region. This region is formed of capacitor plates on the interior top and bottom of the chip, centred on the peak of the acoustic mode-shape.

Figure 2.1 shows the B3 top and bottom chip geometries side by side. After etching and metal deposition these sections would be diced, cleaned, and then directly bonded; such that the etch faces are facing one another and the central capacitors are over one another. A phononic lattice defect mode is isolated within the nanofluidic environment using a regular array of pillars (Figure 2.1 the black etch on the left). The central pillar is not present and an acoustic defect mode is concentrated in the space, also the capacitive region. This concentration of the acoustic and electric fields maximises the overlap integral in (1.21), leading to a much higher g_0 than simple filled cavity resonators [14]. A general outline of the fabrication process is detailed in Appendix A.1.

2.2 Acoustic Lattice

2.2.1 Periodic Acoustic Lattice

COMSOL 5.2 was used to analyse acoustic eigenfrequencies and mode-shapes of potential acoustic lattice geometries. Initially 2D 'pressure acoustics frequency domain' was used to analyse single unit cells with Floquet periodic boundary conditions [15]. Figure 2.2 shows the fundamental 2.07 MHz mode of a square unit cell, side length $a_1 = 100$ μm, with a circular pillar, diameter $a_2 = 80$ μm. Speed of sound $c_h = 255$ ms^{-1} and density 149 kg·m^{-3} of superfluid ^{4}He is used throughout this report.

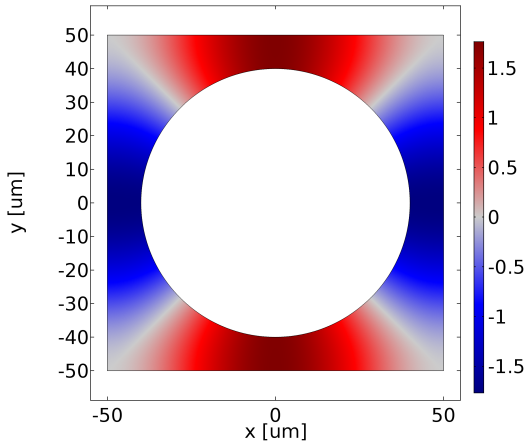

Figure 2.2: The mode-shape function of the fundamental 2.07 MHz mode of a acoustic lattice $a_1 = 100$ μm and $a_2 = 80$ μm, a single brillouin zone of the lattice is shown.

Comparing simulations where soft/hard boundaries are used between the outer helium volume and the cylindrical glass/quartz pillar and also 2D/3D simulations. For expected dimensions, $\sim 100\mu$m$\times 100\mu$m BZ and $100 - 500$ nm depth. No significant diversions from the simplest 2D hard boundary case were found.

Acoustic lattices cause phononic band gap structures. Transmission of acoustic waves of frequencies within these band gaps is forbidden. The band gap structure for an infinite lattice with parameters equal to Figure 2.2 are shown in Figure 2.3.

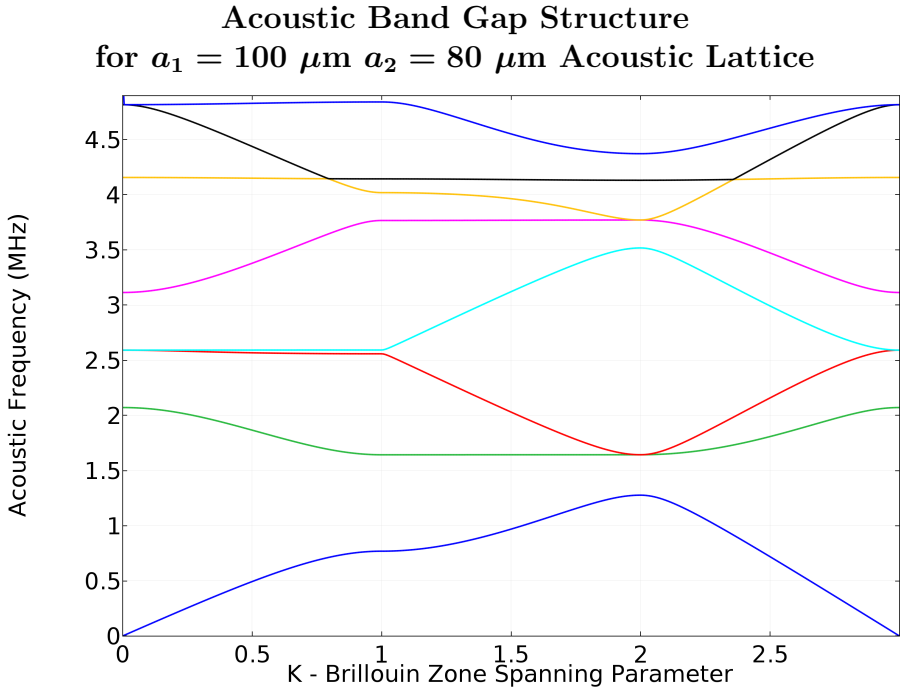

Figure 2.3: The periodic band gap structure of a $a_1 = 100$ μm and $a_2 = 80$ μm unit cell. The brillouin zone spanning k-vector is plotted against acoustic frequency. The first 8 bands are plotted.

This band gap is from ~ 1.28 MHz to ~ 1.64 MHz (between the blue and green lines in Figure 2.3). The larger this band gap the better the isolation of modes contained within. Square lattices with higher ratios of a_2/a_1 were found to give the largest band gaps; with hexagonal lattices giving smaller band gaps for the same value of a_2/a_1. Fabrication limited a_2/a_1 as μm scale wires needed to be deposited in between the pillars, $a_1 = 100$ μm and $a_2 = 80$ μm represent values relatively safe for fabrication.

2.2.2 Lattice Defect Modes

Removing a pillar at the centre of one of these acoustic lattices will cause the formation of a fundamental defect mode within the bad gap region, where acoustic waves are forbidden

from transmission outside of the lattice. These defect modes have the advantages of high Q factors and acoustic energy concentration within the defect region. This method of trapping an acoustic mode is effective even for small $n \times n$ pillar lattices. Finite lattices were analysed with either hard boundaries surrounding them, as in the case of the chip walls enclosing the lattice; or with perfectly matched layers (PML) surrounding, as in the case of helium volumes extending far beyond the lattice. The hard boundary case gives much higher Q factors than the PML, but both cases provide good agreement for acoustic resonant frequency and field concentration within the defect mode. Figure 2.4 shows the defect mode for $a_1 = 100$ μm and $a_2 = 80$ μm, in the hard boundary and PML cases, both have acoustic resonant frequencies of 1.469 MHz.

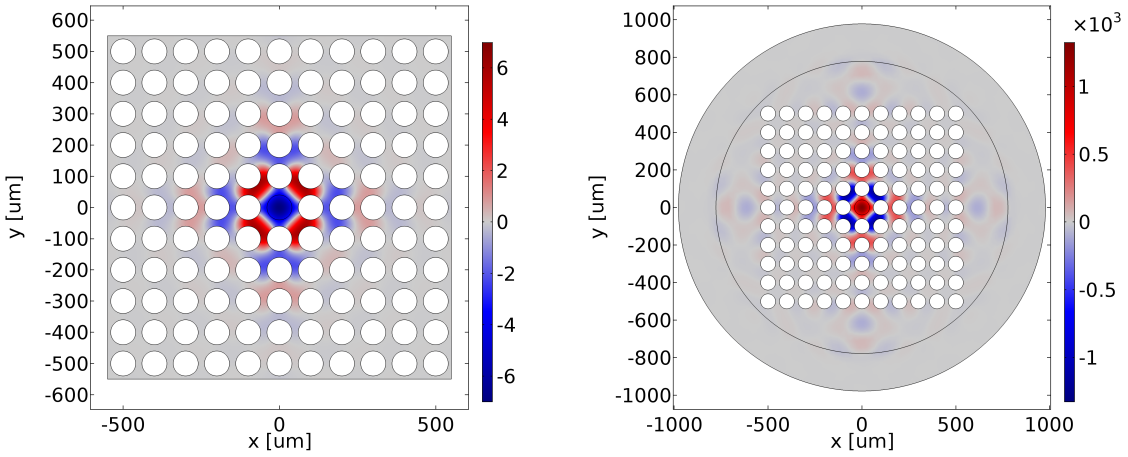

Figure 2.4: 1.469 MHz Acoustic lattice defect modes. Left: The hard boundary case. Right: The PML boundary case, the second circle is the PML. The mode shape extending beyond the lattice is additional acoustic wave propagation against the hard boundary case, this leads to a much lower Q factor.

From simulation, for values of $a_2/a_1 = 0.9$ and larger lattices Q factors exceeding 10^10 are possible. However this assumes perfect superfluid (no attenuation due to friction) and near perfect fabrication. For the geometries discussed coupling of $g_0/2\pi \sim 1$ mHz is expected. To maximise the overlap integral in g_0 capacitor geometry was chosen to overlap with contours of near maximum acoustic field. These contours are shown in Figure 2.5. Due to fabrication alignment accuracy of the top and bottom of the chip, along with etch and deposition alignment, will be a factor in the overlap. Because of this the largest unbroken contour was chosen for the shape of the capacitive elements.

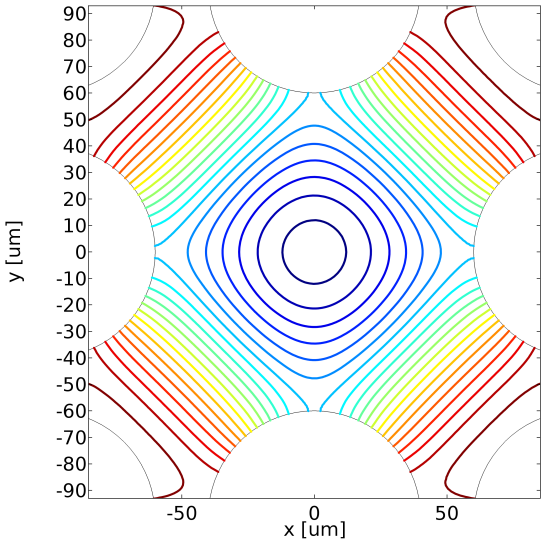

Figure 2.5: The contours of acoustic pressure field around the central lattice defect, for the 1.469 MHz resonant mode. this figure is from the same setup as the hard boundary case in Figure 2.4.

2.2.3 3D Wire Channel Simulation

For expected geometry depths of 100 nm−500 nm and 50 μm−100 μm unit cells, 3D simulations for uniform acoustic lattices give effectively the same results as 2D. However this assumed perfectly fabricated geometry. Therefore simulations were run to assess possible disturbances of acoustic modes, due to metal depositions not lying flush with the top of etched channels.

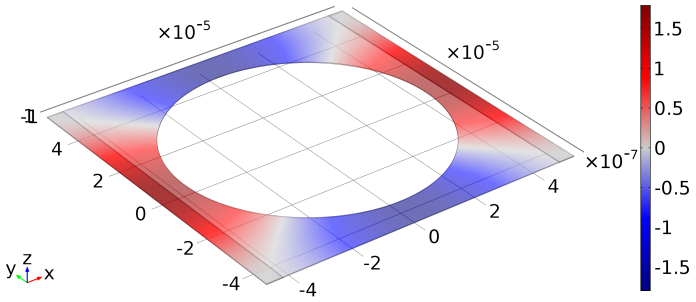

Figure 2.6: Acoustic mode shape for 2.06 MHz fundamental mode for periodic unit cell of acoustic lattice with etched channels. 250 nm deep lattice with 50 nm deep 5 μm wide channels.

Channels either side of the pillar were added to the periodic boundary unit cell simulation. For a range of etch and channel depths, simulations found no significant deviations in the modes or band-gap structures. Figure 2.6 shows the fundamental mode of a 250 nm deep lattice with 50 nm deep 5 μm wide channels, representing a 'worst case scenario', as 50 nm channels were to be etched but then filled via metal deposition. This acoustic resonant mode is at 2.06 MHz, compared to a 2.07 MHz mode in the 'perfect' 2D simulation.

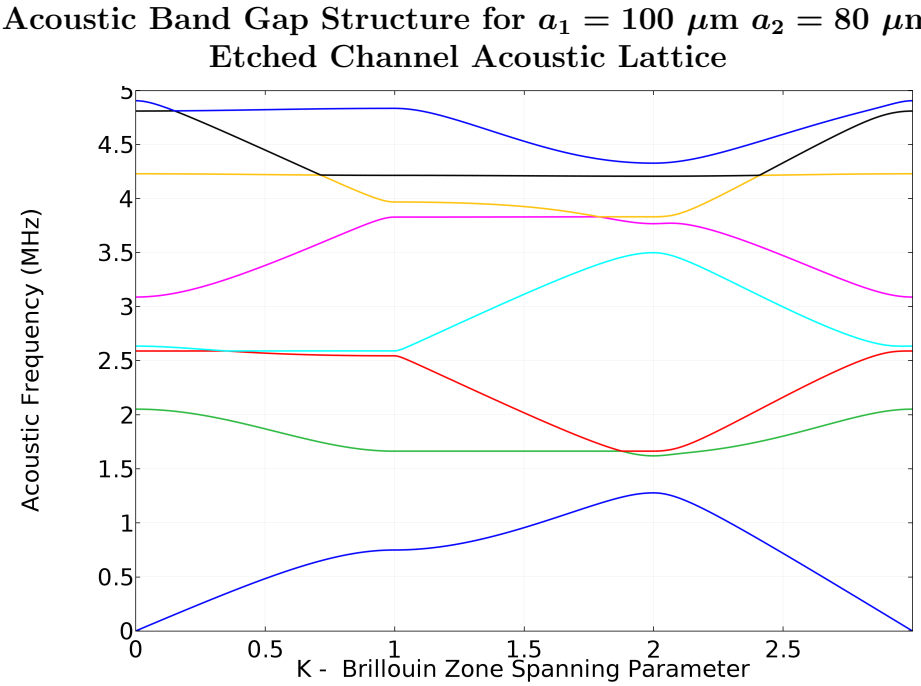

Figure 2.7: Brillouin zone spanning k-vector against acoustic frequency, for the first 8 bands of the 3D etched channel unit cell case.250 nm deep lattice with 50 nm deep 5 μm wide channels.

The band-gap structure of the unit cell in Figure 2.6 is shown in Figure 2.7. Comparing to Figure 2.3, small deviations are present though not significant, and the size of the band-gap is almost unaffected ($\sim$ 1.28 MHz$-$1.62 MHz). This suggests the defect mode will remain well isolated, even in said 'worse case scenario'.

The periodic boundary condition simulation takes into account the wires running through the pillar geometry, but not the effect of imperfections around the electrode. To investigate this etched channels were added to a 3D hard boundary study (a 3D version of Figure 2.4). The key observation of these simulations was the emergence of modes close to the defect mode, with mode-shape concentrated along the wire channels. This is shown in Figure 2.8, for a 100 nm deep lattice with: 50 nm deep 10 μm wide channels, electrode and pillar diameter $a_1 = 80$ μm, and unit cell size 100 μm. The shown mode

is of resonant frequency 1.63 MHz and may contribute to the slight lowering of the top end of the band-gap. Modes form with standing wave structure along the channels, it is therefore possible that the geometry and size of a lattice could create a mode close to the defect mode frequency, which would allow acoustic propagation away from the defect, becoming a major factor of dissipation. This should be considered for future fabrications.

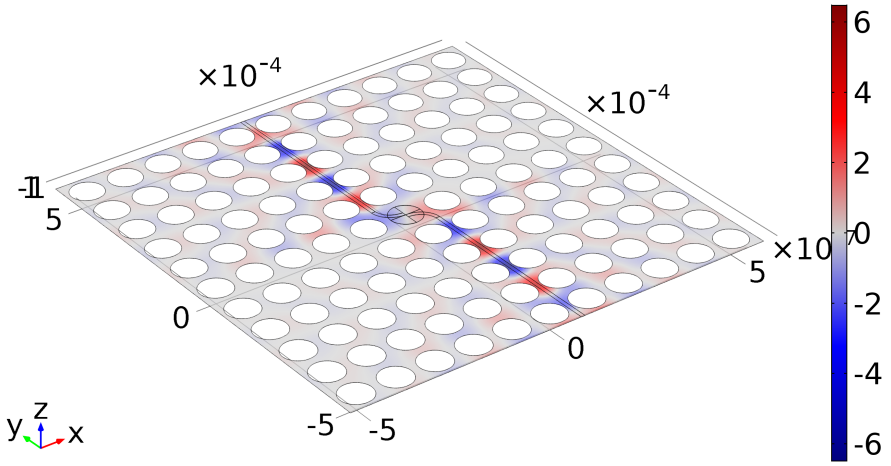

Figure 2.8: Etched channels and capacitive region acoustic defect lattice in the hard boundary case. The 1.63 MHz acoustic resonant frequency mode shape shown is that of acoustic wave propagation, from the outer edge of the lattice to the central capacitive region. For a 100 nm deep lattice with: 50 nm deep 10 μm wide channels, electrode and pillar diameter $a_1 = 80$ μm, and unit cell size 100 μm.

Note for the parameters in Figure 2.8 the resonant frequency is shifted to 1.39 MHz (from 1.47 MHz in Figure 2.4). Though this shift is significant it is for a 100 nm deep lattice and 50 nm deep channels, doubling the size of the central capacitive region. For a 100 nm deep lattice with 10 nm deep channels the defect mode resonant frequency is 1.46 MHz, aligned with the 2D case. These variables are closer to expected errors from fabrication.

2.3 Chipped Microwave Cavity

Simulations were run in COMSOL 5.2 to assess the effect on the electromagnetic field of a rectangular cavity with a chip placed inside. These simulations made use of 'Electromagnetic Waves, Frequency Domain' and neglected the acoustic geometry. Simulations

were initially run with an antenna setup similar to the curent work of Souris *et al.*[16] and Yuan *et al.*[17]. However the antenna, being large flat surfaces, were large sources of edge effects. In experiments by collaborators they did not behave as expected[16]. The focus was shifted to galvanically coupled chips as in the work of Noguchi *et al.* 2016[18], where capacitive antenna coupling is also discussed. The galvanic coupling discussed requires large metal contact pads on fabricated chips, located on the chip regions within the chip holding cavity grooves. Indium is places between these pads and the cavity surface, tightening the cavity presses the indium between these two surfaces, causing an electrical contact between the on chip geometry and cavity itself.

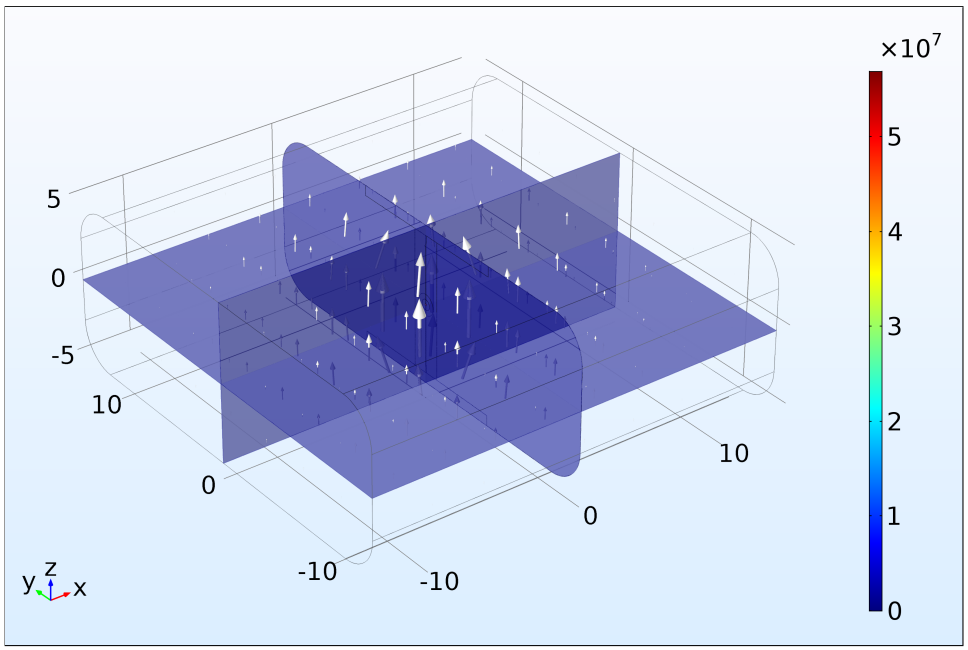

Figure 2.9: The electric field of the TEM_{110} mode, shifted by the presence of centrally located chip geometry. For this size cavity the resonant frequency was originally 7.71 GHz, which has now been shifted to 1.99 GHz, due to 66 μm radius capacitor plates separated by 300 nm

Simulations were run assuming direct connection could be made between the deposited on chip wires and the outside of the cavities. The electric field for one such simulation is shown in Figure 2.9. It was found that the presence of the on chip geometry caused a large frequency shift of the TEM_{110} mode, almost independent of the cavity size and dominated by the capacitance of the central capacitor. This effect was more pronounced with galvanic coupling but still dominant with sufficiently sized antenna. There was also a splitting of the mode for much larger electrodes, where they were sufficiently sized to act as antenna themselves.

Figure 2.10 shows the electric and magnetic fields of a galvanically coupled chip-

cavity system, close to the capacitive chip region. The electric field is concentrated almost entirely between the two plates of the central capacitor, the electric field in this region is 10^7 time greater than that outside. Whilst the magnetic field is concentrated around the wires leading to the capacitive region, pointing in the ϕ direction around the central axis of the wire.

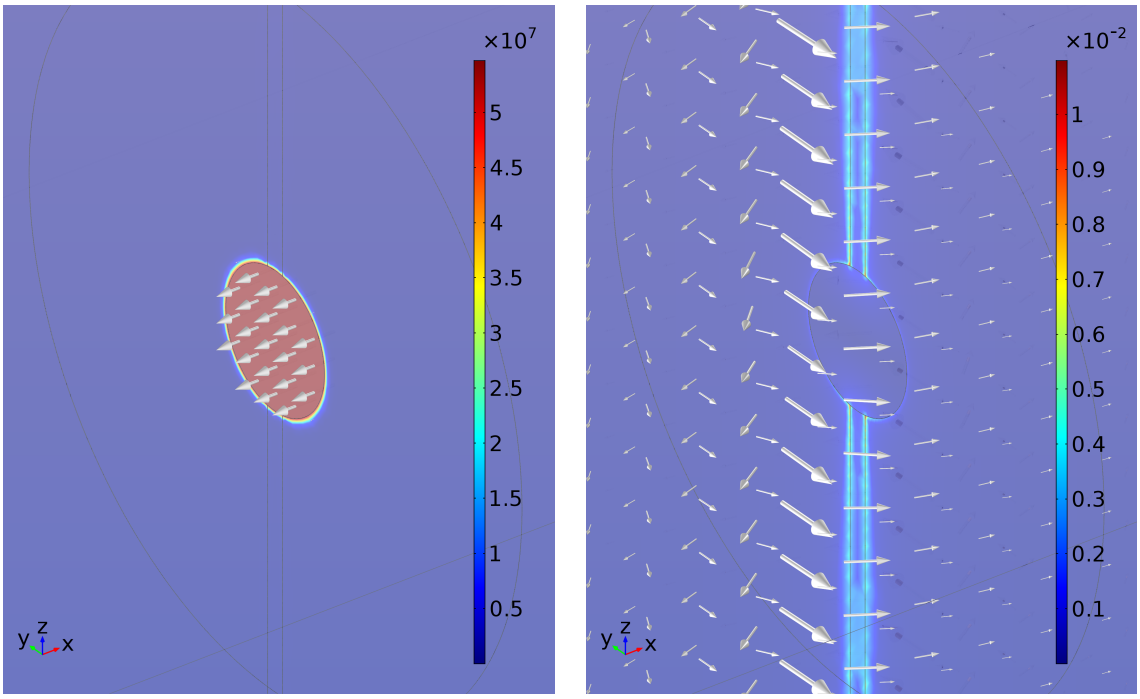

Figure 2.10: Galvanically coupled chip-cavity system, close to the capacitive chip region. Left: Electric field concentrated within capacitive region. Right: Magnetic field concentrated around wires leading to capacitor plates. Arrows show field direction and magnitude.

2.4 Research Trip to UofA

2.4.1 General Considerations

A research trip was undertaken to UofA with the purpose of testing the nanofluidic environments embedded within microwave cavities. A rectangular 16mm×16mm×10mm aluminium cavity was used, with an unperturbed TEM_{110} mode of 13.2 GHz. Technical drawings for this cavity can be found in Appendix A.3. 13mm×12mm×1000μm chips were fabricated at UofA, a table of chip geometries on the associated nano-fabrication masks can also be found in the Appendix A.2, and an outline of the nano-fabrication recipe in Appendix A.1. Two sets of chips were fabricated: one labelled with the prefix B1(), borosilicate chips with an etch depth of 200 nm; the second labelled Q3(), quartz chips with an etch depth of 600 nm. All chips used aluminium for metal geometries. The chips were also labelled with a letter suffix to denote their general type:

- **A:** General chips as discussed in the previous section. Galvanic coupling and large electrodes.
- **B:** Identical in setup to the **A** chips, but with smaller central capacitor plates. e.g. ignore fabrication errors, a chip labelled Q3(B2) would be identical to chip Q3(A2), other than having a smaller capacitive region.
- **C:** These chips were designed to use antenna coupling, in case galvanic coupling proved impossible.
- **D:** Designed to be galvanically coupled but making used of a split ring capacitor rather than parallel plate, because of this the 'bottom' piece of wafer had both galvanic coupling pads and the 'top' only the central circular part of the split ring.

SMA pin and magnetic loops couplings were used, as discussed in [8]. No cavity or chip resonant modes were detected at room temperature. Using a magnetic loop coupler, resonant modes were detected with a heavy dependence on the depth of the loop into the cavity, from simulation these were found to be associated with reflected waves from the opposite surface to the magnetic loop coupler. Simulations were also run to determine the effects on electromagnetic fields of the chip slots and a possible failure of galvanic coupling. No effects significant enough to dominate frequency dependence or mode shape were observed.

The chips were placed inside the cavity with large metal pads overlapping the cavity chip slots. Indium was placed between the pads and cavity surface to provide the galvanic bonding. The cavity was then screwed tight over the chip, pressing the indium against the pads and interiors of the slots. The chipped cavity was then attacked the the bottom of a probe and inserted into a helium fridge. The helium fridge setup consisted of a 1

K closed ^{4}He system with a removable probe. The probe had it's own closed charcoal sorb ^{3}He system to provide additional cooling down to ~ 500 mK. For readout the pin or loop coupler was attached via coaxial SMA cables and a directional coupler to both ports of VNA, effectively measuring the S_{11} parameter. With an appropriate magnitude reference level, the magnitude of the S_{11} parameter was then fitted against [7][19]:

$$|S_{11}| = \sqrt{\frac{(\beta-1)^2 + (2Q_0\delta')^2}{(1+\beta)^2 + (2Q_0\delta')^2}} \tag{2.1}$$

Where β is the input coupling coefficient, Q_0 is the unloaded cavity Q factor and the frequency separation from resonance $\delta' = (f - f_0)/f$, with f_0 being the resonant frequency and f the frequency measure at. From this loaded Q_L and external Q_E quality factors can be calculated:

$$Q_L = \frac{Q_0}{1+\beta} \tag{2.2}$$

$$Q_E = \frac{Q_0}{\beta} \tag{2.3}$$

It is not clear which Q factor the chip will affect, and this model neglects coupling losses. Though it is still useful for categorising the modes. Summaries of the experimental runs will now be discussed.

2.4.2 Run 1: Q3(A3) $f_{expected} = 2.98$GHz

A galvanic coupling run using an SMA pin perpendicular to the chip and centred on the capacitative region. The hope was that this arrangement would allow strong coupling to the central capacitive region via the electric field. However no resonances were observed at any temperature, so the coupling method was switched to magnetic loops for following runs.

2.4.3 Run 2: Q3(A1) $f_{expected} = 5.65$GHz

A loop was created by shortening the outer conductor and dielectric, then bending the conducting core into a loop and soldering the end to the outer conductor. This coupler was inserted centrally, close to the chip and parallel to the on chip wires, the loop itself was positioned above the central capacitive region; with the loop rotated to cut the magnetic field. Attempts were made to fix the loop coupler in place with liquid silver, however these did not prove effective, though the coupler fit tight enough to be reasonably confident it would not move significantly. Warming up, removing the probe, and opening the cavity, found that the chip had broken. It was not clear when the chip had broken;

due to the tightening of the cavity around it, to thermal contraction/expansion, during positioning of the loop, or upon opening the cavity.

2.4.4 Run 3: Q3(B3) $f_{expected} = 5.47$GHz

The same setup was used as in Run 2, although the loop had to be re-soldered as it had come apart. No resonant modes were observed at room temperature. Below roughly 800 mK when the aluminium transitioned to its superconducting state a resonant peak became visible at 7.10 GHz. Figure 2.12 shows the difference between $|S_{11}|$ at 2 K and 500 mK.

Equation (2.1) and the curve_fit function in python were used to fit the data, Figure 2.11 shows $|S_{11}|$ plotted against frequency for the fit and raw data. The fit is in agreement with the data in the peak region. The quality factors: $Q_L = 118$, $Q_0 = 3.14 \times 10^6$ and $Q_E = 118$, were given by the fit. This suggests the magnetic loop coupler is highly over-coupled to the chip mode. This Q_0 is much higher than expected for a chip mode, although not unreasonably. Further analysis is required to determine an effective model for extracting the Q factor of chipped modes. The resonant frequency is significantly higher than expected from simulation. This could be due to many factors; fabrication error, unsuccessful galvanic bonding, the loop coupler itself, or from increased chip separation.

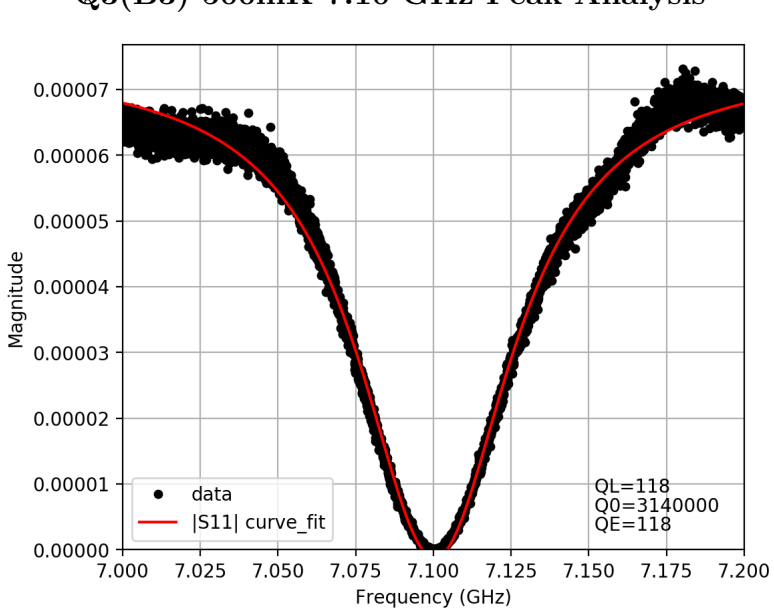

Figure 2.11: Run Q3(B3) at 500 mK, peak analysis around 7.10 GHz peak. Black dots indicating data points and red line the python curve_ fit. Q factors shown bottom right.

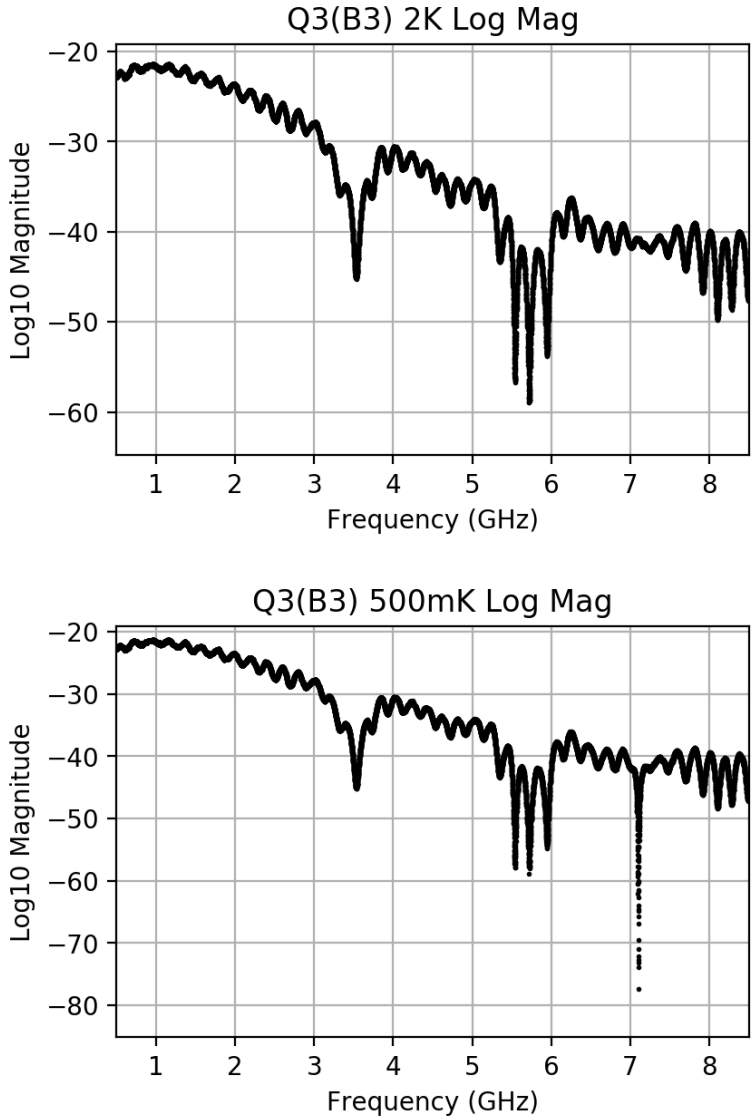

Figure 2.12: For the Q3(B3) run, log magnitude against frequency graphs of data directly from the VNA S_{21} readout (measuring S_{11} of cavity). Top: the frequency spectrum at 2K. Bottom: The frequency spectrum at 500mK.

When the cavity was removed from the chip and opened the chip was again found to be broken, split along the bond. From simulation, if the chip had fully split apart before reaching 500 mK it should not have given a peak at 7.10 GHz (the cavity peak should be relatively unchanged around 13.2 GHz). Suggesting the damage was either caused warming up or when opening the cavity.

2.4.5 Run 4: B1(A1) $f_{expected} = 3.50$GHz

The same setup was used as in run 3, only changing the chip. Again a resonant peak developed once the cavity had cooled below the superconducting transition temperature of aluminium. This peak was at $\sim$ 7.7 GHz, again significantly higher than expected. Analysis of this peak is shown in Figure 2.13.

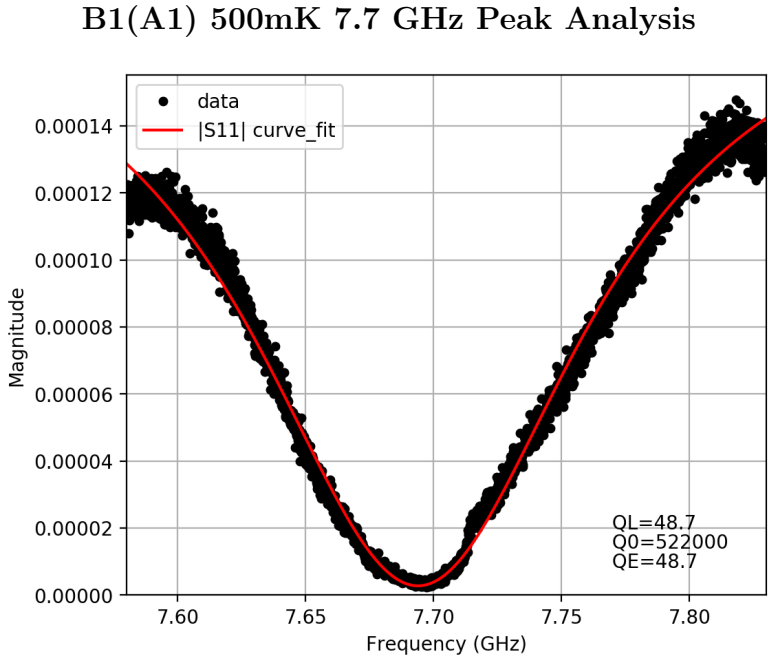

Figure 2.13: Run B1(A1) at 500 mK, peak analysis around 7.7 GHz peak. Black dots indicating data points and red line the python curve_ fit. Q factors shown bottom right.

Quality factors of $Q_L = 48.7$, $Q_0 = 5.22 \times 10^5$ and $Q_E = 48.7$, were given by the fit, suggesting an over-coupled regime. The fit was not in as good an agreement with the data as the previous run, due to a lower Q_L making the peak less defined against background. Again upon warming up and opening the cavity the chip was broken. Extra care was taken to ensure this chip entered the cavity unbroken, and results would suggest it remained intact enough to create a resonance at 500 mK.

2.4.6 Run 5: B1(A3) $f_{expected} = 1.76$GHz

The same setup was used as in run 3 & 4, only changing the chip. A resonant peak developed below the superconducting transition temperature. This peak was at ~ 6.8 GHz, significantly higher than expected. Analysis of this peak is shown in Figure 2.14.

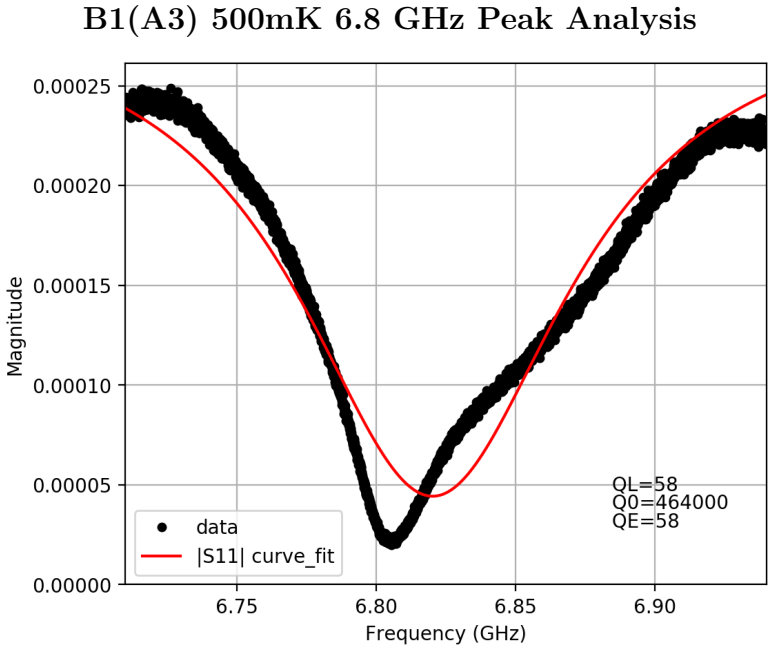

Figure 2.14: Run B1(A3) at 500 mK, peak analysis around 6.8 GHz peak. Black dots indicating data points and red line the python curve_ fit. Q factors shown bottom right.

Quality factors of $Q_L = 58$, $Q_0 = 4.64 \times 10^5$ and $Q_E = 58$, were given by the fit. Again suggesting an over-coupled regime, however this time the fit was not in good agreement with the data, likely due to a low Q_L allowing interference from other spectral features. Again upon warming up and opening the cavity the chip was broken. The chip was observed at all possible stages within the cavity through a hole used for the initial pin coupling. When initially tightening the cavity around the chip, there seemed to be a small misalignment, caused by tightening. This misalignment did not seem to have changed significantly after the cavity had been removed form the fridge. Though when opened the two sides of the chip separated, as with previous runs. Additionally the resonant peaks did not follow an expected pattern, had disturbances be the same on all runs. It is possible that tightening of the cavity was forcing the two sides of the chips to slide out of alignment slightly. This would cause a pseudo random shift in resonant frequency. Though more runs would be required to eliminate other factors.

2.4.7 Research Trip Concluding Remarks

This trip was very useful to learn experimental techniques and gain experience that will be helpful going forward. Few conclusions can be drawn from the data collected, though with relative certainty chip-cavity resonant modes were observed. It did however give insight into refinements of cavities and chips for later experiments. Larger cavities with empty modes detectable by the lab's VNA, focussing on repeatable loop coupling, and with alternative sliding k connectors to replace indium galvanic coupling, will be used in future. Fabrication of chips will need to ensure stronger bonding, or a shift to split ring capacitors to remove the possibility of sheering forces along the chip bond.

It was decided to shift focus from producing chips to test at mK temperatures to testing re-entrant cavities in the hopes of creating a model for the EM fields in future chip-cavity systems. Re-entrant cavities were chosen due to their similar EM field mode shapes, concentrating electric field between two capacitive elements, and magnetic field around a longer inductive element. Both analogous to coaxial cables terminated in capacitors.

Chapter 3:

Re-entrant Cavity Approach

3.1 Re-entrant modes:

Figure 3.1: Left: Electric field norm of 2D axisymmetric cross section of a cylindrical re-entrant cavity fundamental mode. Right: Magnetic field norm of a cylindrical re-entrant cavity fundamental mode. Arrows show field direction and strength. The fillet at the top of the pillar is to remove edge effects and the one at the bottom to provide stability. *(note: in comsol to get the B field arrows use imag(B) and rev1phi to transform coordinates)*

A general re-entrant cavity differs from a normal microwave cavity by having a re-entrant 'stub' or 'pillar' which extends form one of the interior surface, made from the same material as the cavity itself. This stub usually extends close to the opposite interior surface and is terminated in a flat circle (with filleted edges to prevent edge effects). Provided the stub sits close enough to the opposite surface, the electric field of the fundamental mode will be concentrated almost entirely in the region between these two surfaces, forming a 'capacitive' region. Focusing on relatively uniform cylindrical 'pillar' cavities rather than curved 'stub' cavities. The lumped element analogy is straightforward with a uniform pillar, and more relevant to later optomechanics studies. In this case the magnetic field of this fundamental mode is concentrated around the pillar in the $\pm\phi$ direction. Both the electric and magnetic fields of the fundamental mode are shown in Figure 3.1.

3.2 Lumped Element Circuit Approach:

3.2.1 Generic 'Resonator' Cavity Approach:

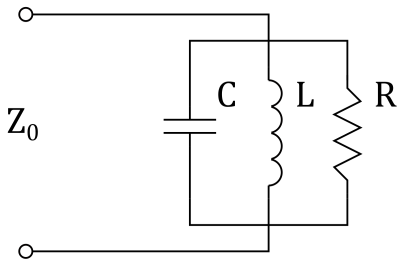

Figure 3.2: A simple diagram of a parallel RLC circuit terminated in impedance Z_0.

Any cavity can be generalised to an RLC resonator lumped element, in either series or parallel equivalent representations. The parallel arrangement is shown in Figure 3.2.

A simple equation for the resonant frequency of an RLC circuit is:

$$f_0 = \omega_0/2\pi = \frac{1}{2\pi\sqrt{LC}} \tag{3.1}$$

Where L is the inductance and C the capacitance. Using (5) and the knowledge that on resonance energy stored in the electric field is equal to energy stored in the magnetic, the L and C parameters can be written in terms of the TEM modes as:

$$L_{mnl} = \mu k_{mnl}^2 V \tag{3.2}$$

$$C_{mnl} = \frac{\epsilon}{k_{mnl}^4 V} \tag{3.3}$$

Where V is the volume, mnl the mode number, μ the absolute magnetic permeability and ϵ the absolute permittivity.

3.2.2 Re-entrant Capacitor Terminated Coax

The RLC analogy holds for a re-entrant cavity, as the RLC model can be used for a generic 'resonator' circuit element. However the equations for L_{mnl} and C_{mnl} will not hold true as the re-entrant cavity does not have pure TEM modes. However the entire cavity can be modelled as a coaxial cable terminated in a capacitor (Figure 3.3), if it can be approximated to: a cylindrical cavity, cylindrical pillar, and a small enough gap to concentrate the electric field to the capacitive region.

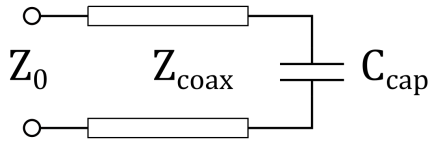

Figure 3.3: A simple diagram of a coaxial cable impedance Z_{coax} terminated in a capacitor of capacitance C_{cap} and connected to an outside line impedance Z_0.

This simple diagram is useful but the circuit can be redrawn in a way analogous to the RLC circuit, where the L and C parameters can be calculated. Figure 3.4 shows a diagram for the dimensions of a re-entrant cell, along with this RLC representation. The assumption has been made that the bulk of the magnetic field can be considered within the coax element, therefore only the coaxial inductance is present. For smaller caps C_{cap} is also dominant.

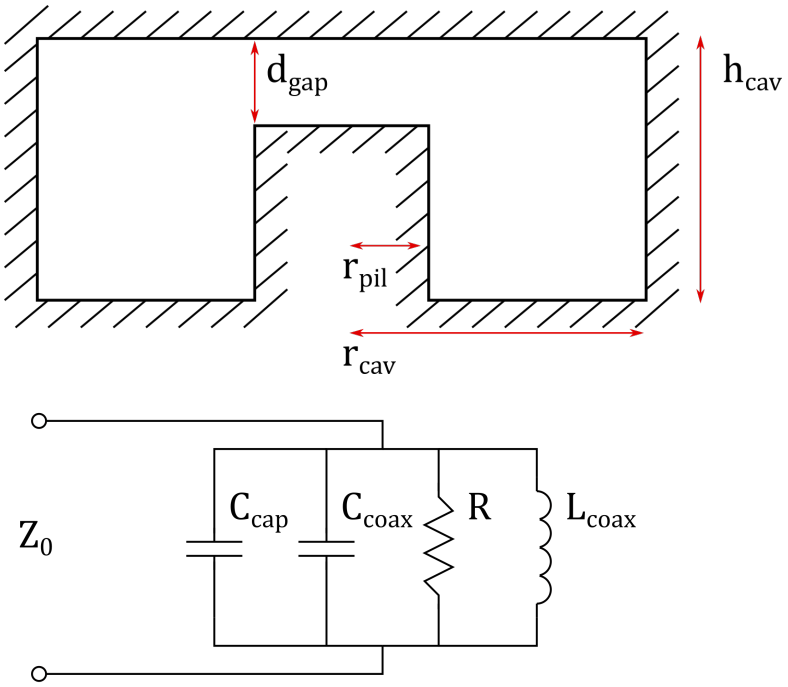

Figure 3.4: Top: diagram with labelled dimensions of a simple cylindrical re-entrant cavity. Bottom: A circuit diagram of a re-entrant cavity as an equivalent RLC circuit, terminated in impedance Z_0.

Assuming a linear electric field in the gap, the equation for a parallel capacitor can be used for the terminating capacitance:

$$C_{cap} = 2\pi\epsilon r_{pil}^2/d_{gap} \tag{3.4}$$

Where r_{pil} is the radius of the re-entrant pillar and d_{gap} is it's distance to from the opposing surface. A more complicated version of this for tapered pillars is in [20]. Using the standard equations for a coaxial cable we can write the coax capacitance:

$$C_{coax} = \frac{2\pi\epsilon h_{cav}}{\ln(r_{cav}/r_{pil})} \tag{3.5}$$

Where h_{cav} is the height of the cavity (length of the coax) and r_{cav} is the radius of the cavity (outer radius of the coax). This can then be related to a generic RLC cavity with $C = C_{cap} + C_{coax}$. We can also write the coaxial inductance:

$$L_{coax} = \frac{\mu h_{cav}}{2\pi}\ln(r_{cav}/r_{pil}) \tag{3.6}$$

With all terms defined as previously. Note if you assume the internal system is lossless $Z_{coax} = \sqrt{L/C}$, in practise there will be some internal and some external losses. Internal losses for re-entrant cavities have not been greatly explored (see later reports for discussion).

3.3 COMSOL Approach

As discussed previously it was decided to focus on cylindrical re-entrant pillar cavities. To find the optimal parameters to maximise possible g_0 COMSOL Multiphysics 5.2 was used. The 'Pressure Acoustics, Frequency Domain (acpr)' and 'Electromagnetic Waves, Frequency Domain (emw)' physics interfaces were used to analyse a 2D axisymmetric model. The two physics interfaces were used within separate 'studies' as their interaction was expected to be expressed by g_0 alone, at least to the first order.

After basic analysis, parameter sweeps to find acoustic and electromagnetic (EM) eigenfrequencies were computed for: cavity radius, cavity height, pillar-surface gap and pillar radius. All combinations of these sweeps were analysed. Coupling to the fundamental EM mode was being investigated, therefore the EM sweep was setup to find the first eigenfrequency above 1GHz. For the acoustics the first 20 resonant modes above 9kHz were found, these cutoffs were used to ignore the low frequency modes generated by finite element meshing.

Once COMSOL had solved for these modes, g_0 was determined for each acoustic mode, matched in sets of 20 to an EM mode and set of cavity parameters. To collate variables from different solutions the command *withsol()* was used. For example to pull ω_c into an equation using acoustic mode solutions *withsol('sol10', emw.freq, setval(r_cav,*

r_cav, ...)) was used. Where *sol10* was the EM parameter sweep solution, and *setval(a,b)* causes *withsol()* to pull *emw.freq* for the value of b for the parameter a. Therefore having *setval(a,a)* gives the same value of a as the parameter set in the current acoustic eigenvalue solution.

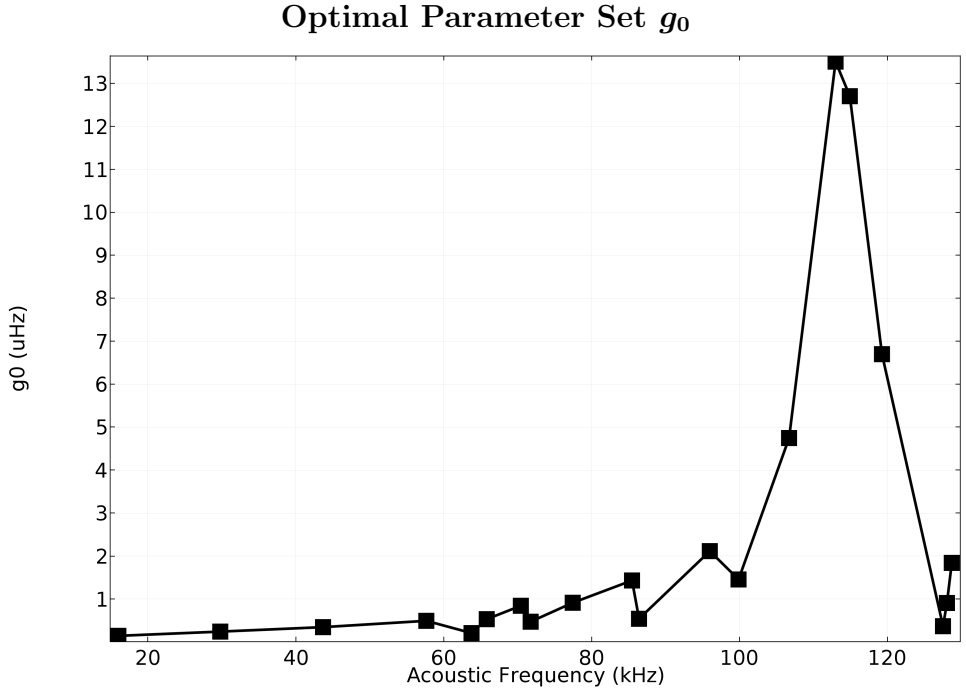

Figure 3.5: g_0 against acoustic resonance frequency for the optimal parameter set from the full sweep, each point corresponds to one of the twenty computed acoustic resonance modes.

Solution number for maximum g_0 can be read off then checked against the ordering of parameter sweeps to find the optimal parameter set. This was found to be: $r_{pil} = 1$ mm, $d_{gap} = 10$ μm, $h_{cav} = 2$ mm and $r_{cav} = 10$mm. Additionally a value of 0.25 mm was chosen for the top of pillar fillet, and 0.5 mm for the bottom, as an approximation to fabricated cavities.

For the set of optimal parameters a plot of acoustic resonant frequency against g_0 is shown below in Figure 3.5. Similar to the TEM rectangular modes, increasing frequency acoustic modes have increasing numbers of nodes in both the r and z directions. However unlike EM modes an anti-node can be placed at the cavity edges/corners. As the electric field is concentrated in the gap region (Figure 3.1), acoustic pressure being concentrated into the same region will give a higher value of the overlap function and therefore a higher g_0. In general this happens for higher frequency modes with an anti-node at the gap region, the highest g_0 mode is shown in Figure 3.6. This concentration of acoustic field also reduces the effective volume of the mode which is inversely proportional to g_0. This is also why higher factors of g_0 are expected than standard cavity resonators [14].

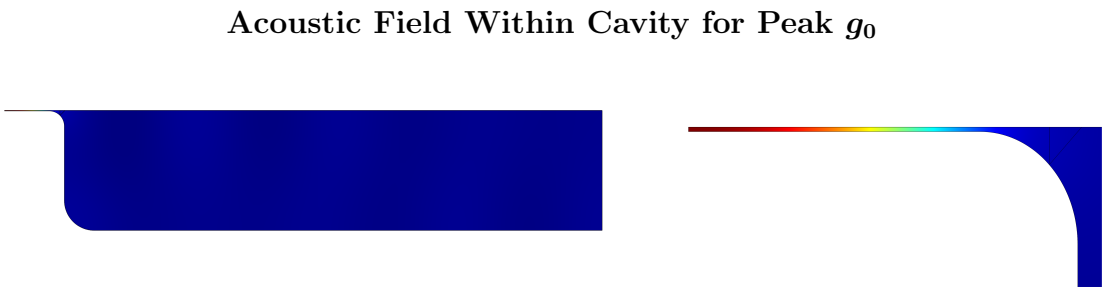

Figure 3.6: Acoustic pressure field plot for peak g_0 113 kHz acoustic mode, within the optimal parameter set. Left: Full mode. Right: Acoustic field within gap region

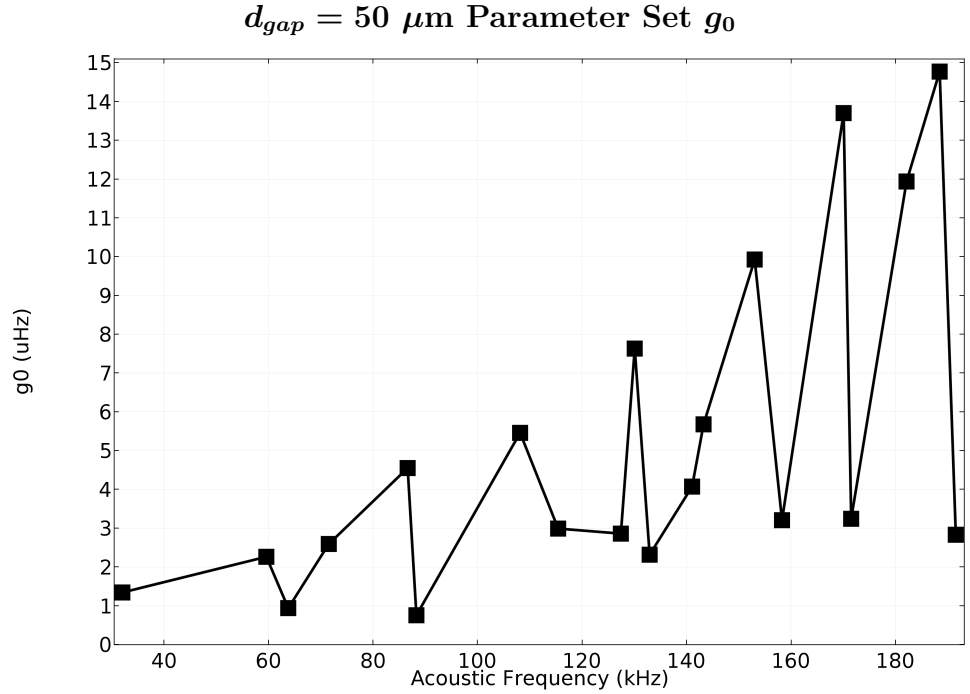

Figure 3.7: g_0 against acoustic resonance frequency for the optimal parameter set from the $d_{gap} = 50$ μm sweep, each point is an acoustic resonance mode.

There is a balance between concentration to the centre of the cavity, which reduces the effective volume of the mode; and matching to the electric field, which increases the overlap function. Therefore at higher frequencies g_0 begins to decrease as the acoustic mode shape is concentrated to the very centre of the capacitive region. At even higher frequencies the concentrative effect can break down, and the modes begin spreading more evenly across the volume.

Machining of a 10 μm gap accurately was not possible, leaving the possibility of a gap with a high percentage error, which could prove an issue in later testing. Therefore a second cavity was fabricated with a 50 μm gap. The same COMSOL program was run but with d_{gap} fixed at 50 μm, the optimal parameters for this gap size were found to be: r_{pil} = 0.5 mm, h_{cav} = 2 mm and r_{cav} = 5 mm. The larger gap for this cavity gives a much sharper contrast between having a node and anti-node at the centre of the cavity, as shown by the peaks and troughs in Figure 3.7.

3.4 Comparison Of Fabricated Cavities

The dimensions of the two cavities are summarised in Table 3.1 below. In general a smaller d_{gap} gave a higher coupling constant, likely due to a much smaller effective mode mass. Shallower low h_{cav} cavities also gave lower g_0, though by a much smaller factor. The dimensions did not affect g_0 independently, especially r_{pil} and r_{cav} where a balance to concentrate the acoustic field over the entire capacitor region was required to maximise g_0.

Table 3.1: Comparison of Fabricated Cavity Dimensions and Resonance Attributes

d_{gap} (μm)	r_{pil} (mm)	h_{cav} (mm)	r_{cav} (mm)	ω_c /2π (GHz)	Ω_m /2π (kHz)	V_{eff} (mm^3)	g_0 /2π (μHz)
10	1	2	10	3.46	113	0.0157	13.5
50	0.5	2	5	12.2	188	0.172	14.8

Initially a minimum r_{cav} of 10 mm was used, as the SMA pins being used have an outer dielectric diameter of 4.06 mm, so holes for ports would interfere with the modes. However for the safer d_{gap} = 50 μm cavity the dielectric will be trimmed down, and a 2 mm diameter port used. This may produce additional noise due to the change in impedance between the standard SMA line and port.

The resonant frequencies and associated attributes of the cavities are also summarised in Table 3.1. As expected a larger gap gives higher EM resonant frequency (dominated by capacitance) and effective mass. However unexpectedly a slightly higher g_0 is predicted; although 12.2 GHz is pushing the top end of resolvable frequencies, and

the low r_{cav} may make it difficult to couple to the EM mode without disturbing it, or the acoustic mode.

Comparison of the resonant frequencies predicted by COMSOL and the capacitor terminated coax are show below in Table 3.2:

Table 3.2: Comparison of Fabricated Cavity Dimensions and resonance Attributes

d_{gap} (μm)	ω_{comsol} $/2\pi$ (GHz)	C (pF)	L (pH)	ω_{coax} $/2\pi$ (GHz)
10	3.46	5.61	916	2.21
50	12.2	0.33	916	9.17

The EM resonant frequencies predicted by the simple capacitor terminated coaxial cable model are in relative agreement with those predicted by COMSOL, the discrepancy is likely due to the curvature at the top and bottom on the pillar being present in only the COMSOL model. From experience COMSOL gives good agreement with physical testing ($\approx$ 10% error). This indicates the coax model is a useful tool for predicting resonances and also cavity response via LC parameters. The R parameter is more difficult to estimate, as it will be primarily determined by quality of fabrication and is easier to assess physically. Technical drawings for both cavities can be found in Appendix B.2 and B.3.

3.5 Future Work

Work will continue on re-entrant microwave cavities, with the hope of developing a system for modelling chip-cavity geometries in a similar way. This work will begin at room temperature, then transition to lower temperatures as the cavities themselves are developed, alongside 1 K and mK systems. Nano-fabrication skills and techniques will be developed for the second generation of chips. Simulation will continue in parallel to experimental work. More specific extensions are:

- **Characterise 1st generation of re-entrant cavities:** Tests of resonances for two cavities discussed earlier in this chapters, extended from simple VNA analysis to a microwave interferometer setup.
- **Characterisation of indium seal height effects:** Indium seals will be required in low temperature experiments [21], for re-entrant cavities a simple o-ring will affect the height of the gap. This either needs to be taken into account, or a seal devised which does not affect vertical height.

- **Investigate superconducting plating for copper cavities:** It is possible to deposit a thin layer of superconducting metal onto a copper cavity[22]. This may simplify creation of superconducting cavities, and also allow control of re-entrant gap sizes.

- **Investigate optomechanics with re-entrant cavities:** There are a few choices for working a mechanical resonator into a re-entrant cavity. The cavity can be filled with liquid (as discussed in this chapter), the lid can be thinned above the pillar to create a membrane with mechanical modes, or the pillar itself can be lengthened to act like a clamped beam.

- **Develop readout pillar:** Arrays of re-entrant stubs with interacting modes can be used within cavities[23]. It may be possible to use one pillar to 'readout' a changing state on the other, this could then be used in conjunction with a chip, eliminating the difficulty of coupling electromagnetically to the chip mode.

- **Develop stronger bonded chips:** Chips breaking was a significant issue, preventing repeated testing. From the experimental runs it appears as though chips did not break purely from thermal expansion/contraction. It is possible improvements to cavity design and galvanic coupling could eliminate this issue. Bonding strength could also be improved, which is heavily dependent on how clean the surfaces of the substrates are. For this initial fabrication run, completely removing the bilayer photoresist proved difficult (Appendix A.1). A higher temperature PG remover may solve this issue, additionally using heat and/or pressure could create a stronger bond [24].

Bibliography

[1] J. Kepler, "De cometis," *Libelli tres. Mylius: Augustae Vindelicorum*, vol. 1619.

[2] S. Stenholm, "The semiclassical theory of laser cooling," *Rev. Mod. Phys.*, vol. 58, pp. 699–739, Jul 1986.

[3] J. Aasi, J. Abadie, B. Abbott, R. Abbott, T. Abbott, M. Abernathy, C. Adams, T. Adams, P. Addesso, R. Adhikari, *et al.*, "Enhanced sensitivity of the ligo gravitational wave detector by using squeezed states of light," *Nature Photonics*, vol. 7, no. 8, p. 613, 2013.

[4] A. D. O'Connell, M. Hofheinz, M. Ansmann, R. C. Bialczak, M. Lenander, E. Lucero, M. Neeley, D. Sank, H. Wang, M. Weides, *et al.*, "Quantum ground state and single-phonon control of a mechanical resonator," *Nature*, vol. 464, no. 7289, p. 697, 2010.

[5] M. Li, W. Pernice, C. Xiong, T. Baehr-Jones, M. Hochberg, and H. Tang, "Harnessing optical forces in integrated photonic circuits," *Nature*, vol. 456, no. 7221, p. 480, 2008.

[6] M. Kang, A. Nazarkin, A. Brenn, and P. S. J. Russell, "Tightly trapped acoustic phonons in photonic crystal fibres as highly nonlinear artificial raman oscillators," *Nature Physics*, vol. 5, no. 4, p. 276, 2009.

[7] D. M. Pozar, *Microwave engineering*. John Wiley & Sons, 2009.

[8] M. J. Reagor, *Superconducting cavities for circuit quantum electrodynamics*. Yale University, 2016.

[9] T. L. Brecht, *Micromachined quantum circuits*. PhD thesis, Yale University, 2017.

[10] M. Aspelmeyer, T. J. Kippenberg, and F. Marquardt, "Cavity optomechanics," *Reviews of Modern Physics*, vol. 86, no. 4, p. 1391, 2014.

[11] E. Talebian and M. Talebian, "A general review on the derivation of clausius–mossotti relation," *Optik-International Journal for Light and Electron Optics*, vol. 124, no. 16, pp. 2324–2326, 2013.

[12] B. Hauer, C. Doolin, K. Beach, and J. Davis, "A general procedure for thermomechanical calibration of nano/micro-mechanical resonators," *Annals of Physics*, vol. 339, pp. 181–207, 2013.

[13] S. W. Rienstra and A. Hirschberg, "An introduction to acoustics," *Eindhoven University of Technology*, vol. 18, p. 19, 2004.

[14] L. A. De Lorenzo, *Optomechanics with superfluid helium-4*. PhD thesis, California Institute of Technology, 2016.

[15] P. A. Deymier, *Acoustic metamaterials and phononic crystals*, vol. 173. Springer Science & Business Media, 2013.

[16] F. Souris. private communication.

[17] M. Yuan, V. Singh, Y. M. Blanter, and G. A. Steele, "Large cooperativity and microkelvin cooling with a three-dimensional optomechanical cavity," *Nature communications*, vol. 6, p. 8491, 2015.

[18] A. Noguchi, R. Yamazaki, M. Ataka, H. Fujita, Y. Tabuchi, T. Ishikawa, K. Usami, and Y. Nakamura, "Ground state cooling of a quantum electromechanical system with a silicon nitride membrane in a 3d loop-gap cavity," *New Journal of Physics*, vol. 18, no. 10, p. 103036, 2016.

[19] J. Aitken, "Swept-frequency microwave q-factor measurement," in *Proceedings of the Institution of Electrical Engineers*, vol. 123, pp. 855–862, IET, 1976.

[20] J. Barroso, P. Castro, O. Aguiar, and L. Carneiro, "Reentrant cavities as electromechanical transducers," *Review of scientific instruments*, vol. 75, no. 4, pp. 1000–1005, 2004.

[21] C. Lim, "Indium seals for low-temperature and moderate-pressure applications," *Review of scientific instruments*, vol. 57, no. 1, pp. 108–114, 1986.

[22] D. F. Bogorin, D. T. McClure, M. Ware, and B. Plourde, "Copper waveguide cavities with reduced surface loss for coupling to superconducting qubits," *IEEE Transactions on Applied Superconductivity*, vol. 24, no. 4, pp. 1–7, 2014.

[23] M. Goryachev and M. E. Tobar, "Creating tuneable microwave media from a two-dimensional lattice of re-entrant posts," *Journal of Applied Physics*, vol. 118, no. 20, p. 204504, 2015.

[24] P. Mao and J. Han, "Fabrication and characterization of 20 nm planar nanofluidic channels by glass–glass and glass–silicon bonding," *Lab on a Chip*, vol. 5, no. 8, pp. 837–844, 2005.

[25] B. C. Coalmon, “Cnst nanolithography toolbox,” 2016.

Appendices

Appendix A: Research Trip to University of Alberta

A.1 Nano-Fabrication Recipe Outline

As discussed previously chips were fabricated onto quartz and borosilicate wafers. The chips were fabricated in halves and then bonded together to create a near-2D acoustic defect lattice between them, Figure 2.1 shows the design of the B3 top and bottom sections in KLayout. The bonded chips were 13mm×12mm×1000μm, falling into 3 categorises described in subsection 2.4.1. An outline of the fabrication process is as follows:

1. **Design Masks:** Photomasks were designed using the CNST Nano-Lithography Toolbox [25], and viewed on KLayout.
2. **Order Masks:** Three masks were ordered, one defining the 2D pillar geometry, one defining the channel geometry for metal deposition, and the last for defining the area for metal deposition.
3. **Clean wafers:** With piranha, then rinsing with DI water.
4. **Lithography 1:** For the 2D geometry. HMDS deposition to improve cohesion of resit when spinning. Then in order: Spin resist, bake, expose and develop.
5. **Etch:** Either glass or quartz depending on the wafer. A dry etch was used to better obtain vertical walls, though possible increased surface roughness. One of two etchers were used, the Alcatel ICPRIE and the RIE Trion.
6. **Strip Photo Resist**
7. **Measure Etch Depth:** Using Alpha Step IQ.
8. **Lithography 2:** For the channels into which metal deposition will occur. To align with the previous lithography the SUSS Microtech MA/BA 6 mask and bond aligner was used. After the alignment the steps are the same as Alignment 1.
9. **Repeat Steps 5-7**
10. **Piranha Clean**
11. **Lithography 3:** To define region for metal deposition. Two layer resist was used to facilitate lift off. In order the steps are: HMDS deposition, spin LOR5B, bake, spin HPR504, expose HPR504, develop HPR504, post bake, cool and rehydrate, develop LOR5B.

12. **Metal Deposition:** 50 nm layer of aluminium deposited. Using either sputtering or evaporation. Evaporation giving better lift off.
13. **Lift Off:** Using PG remover overnight, better results with heating and ultrasound.
14. **Characterisation:** Profilometry and optical inspection.
15. **Dicing:** Protective resist applied before dicing with saw, then stripped after.
16. **Imaging:** FESEM, SEM and Helium Ion Microscope. FESEM most effective.
17. **Bonding:** Piranha then plasma cleaning. ABM mask aligner was used to align the top and bottom substrates. One piece being plated on the bottom chuck, and the other being attached to the underside of a piece of blue tape, which covers a home-made frame mounted on the mask aligner. Reasonable alignment was achieved using the mask aligners optical microscope and the substrate bonding alignment marks. Once aligned the chuck was raised exerting pressure between the two chips, which were then pressed down upon by hand, bonding them together.

As Discussed in subsection 2.4.1 two sets of chips were fabricated: one labelled with the prefix B1(), borosilicate chips with an etch depth of 200 nm; the second labelled Q3(), quartz chips with an etch depth of 600 nm.

A.2 Table of Chip Dimensions

Parameters:

- $\boldsymbol{a_1}$: Unit cell width.
- $\boldsymbol{a_2}$: Pillar diameter.
- $\boldsymbol{e_l}$: Electrode side length.
- $\boldsymbol{w_{il}}$: Wire width inside lattice.
- $\boldsymbol{w_g}$: Wire groove inside lattice.
- $\boldsymbol{w_{ol}}$: Wire width outside lattice.
- $\boldsymbol{\omega_{100}}$: Expected frequency with 100 nm capacitor gap.
- $\boldsymbol{\omega_{500}}$: Expected frequency with 500 nm capacitor gap (cavity dimensions for both assumed to be 27 mm×27 mm×10 mm).

Table A.1: Comparison of Chip Dimensions and expected resonances in 27 mm×27 mm×10 mm

Chip:	a_1 (μm)	a_2 (μm)	e_l (μm)	w_{il} (μm)	w_g (μm)	ω_{100} (GHz)	ω_{500} (GHz)
A1	100	70	60	10	20	2.41	4.85
A2	100	80	60	10	15	2.41	4.85
A3	200	160	120	20	30	1.20	2.98
A4	200	180	120	10	15	1.16	2.53
A5	50	40	30	4	7	4.55	6.87
B1	100	70	30	10	20	4.48	6.86
B2	100	80	30	10	15	4.48	6.86
B3	200	160	60	20	30	2.35	4.73
B4	200	180	60	10	15	2.27	4.63
C1	100	80	60	10	15	4.14	6.02
C2	200	180	120	10	15	3.35	4.20
C3	50	40	30	4	7	5.80	7.31
C4	100	80	30	10	15	5.71	7.29
D1	100	80	60	10	15	4.63	6.94
D2	200	180	120	10	15	2.33	4.72
D3	200	180	120	10	15	2.53	5.01
D4	50	40	30	4	7	6.79	7.45

A.3 Microwave Cavity

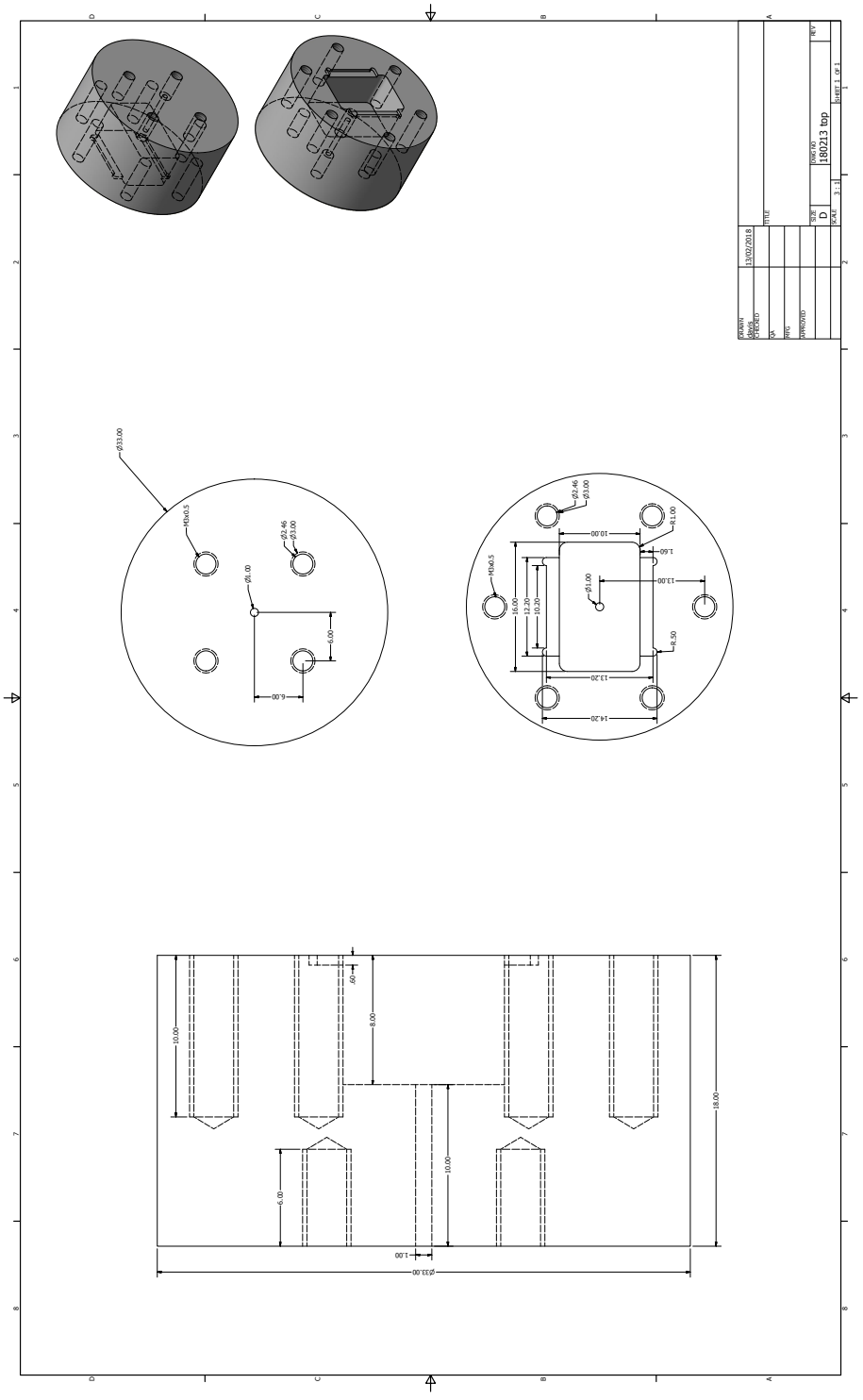

Figure A.1: Top of cavity used to test chips at University of Alberta.

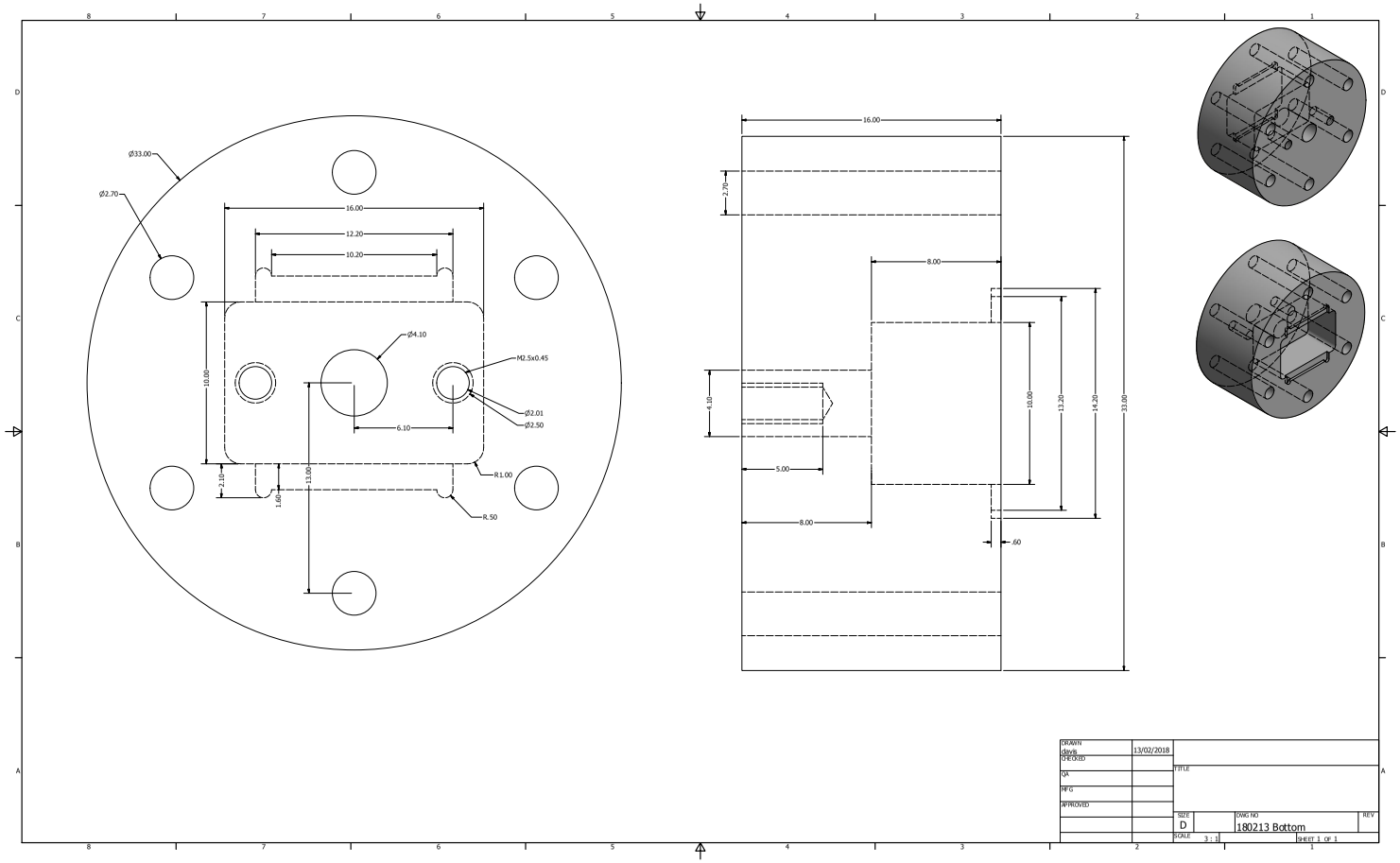

Figure A.2: Bottom of cavity used to test chips at University of Alberta.

Appendix B: Re-entrant Cavities

B.1 Physical Cavity Attributes

See in Appendices B and C technical drawings of the optimal and safe re-entrant cavities. This section will cover some fabrication details not specific to the physics. The additional features:

- **Indium O-ring:** this 1mm wide 0.5mm deep circular groove around the bottom of the cavity is for the indium seal if the cavity were to be filled with superfluid helium.
- **Vacuum Port/Fill line:** the 2mm diameter narrowing into 0.5mm diameter hole in both tops is to allow the cavity to be pumped to vacuum, or for a fill line to be fitted. The narrowing was necessary as a 0.5mm hole could only be fabricated through 3mm of the oxygen free copper.
- **SMA Fitting:** The 4.1mm diameter hole with M2.5x0.45 screw holes either size is for a standard SMA pin to be attached to the cavity for the purpose of coupling to the EM modes. This was narrowed on the safe design to allow the pin/loop to sit nearer the outside of the cylinder. The 1mm indent before narrowing was to ensure contact between the outside of the SMA and the cavity, in case the dielectric was not shortened to be flush.
- **Screw Holes for Seal Breaking:** the M2.5x0.45 through holes in the tops are for screws to press onto the bottom of the cavity to break the indium seal when the cavity needs to be opened.
- **Outer Flange:** This outer flange with 6 through holes is to attached the cavity to either a grounding plate or to a probe.
- **Pillar Bottom Fillet:** the bottom of the re-entrant stub was filleted to allow easier fabrication and reduce risk of pillar vibrational modes.

B.2 Optimal Re-entrant Cavity Drawing

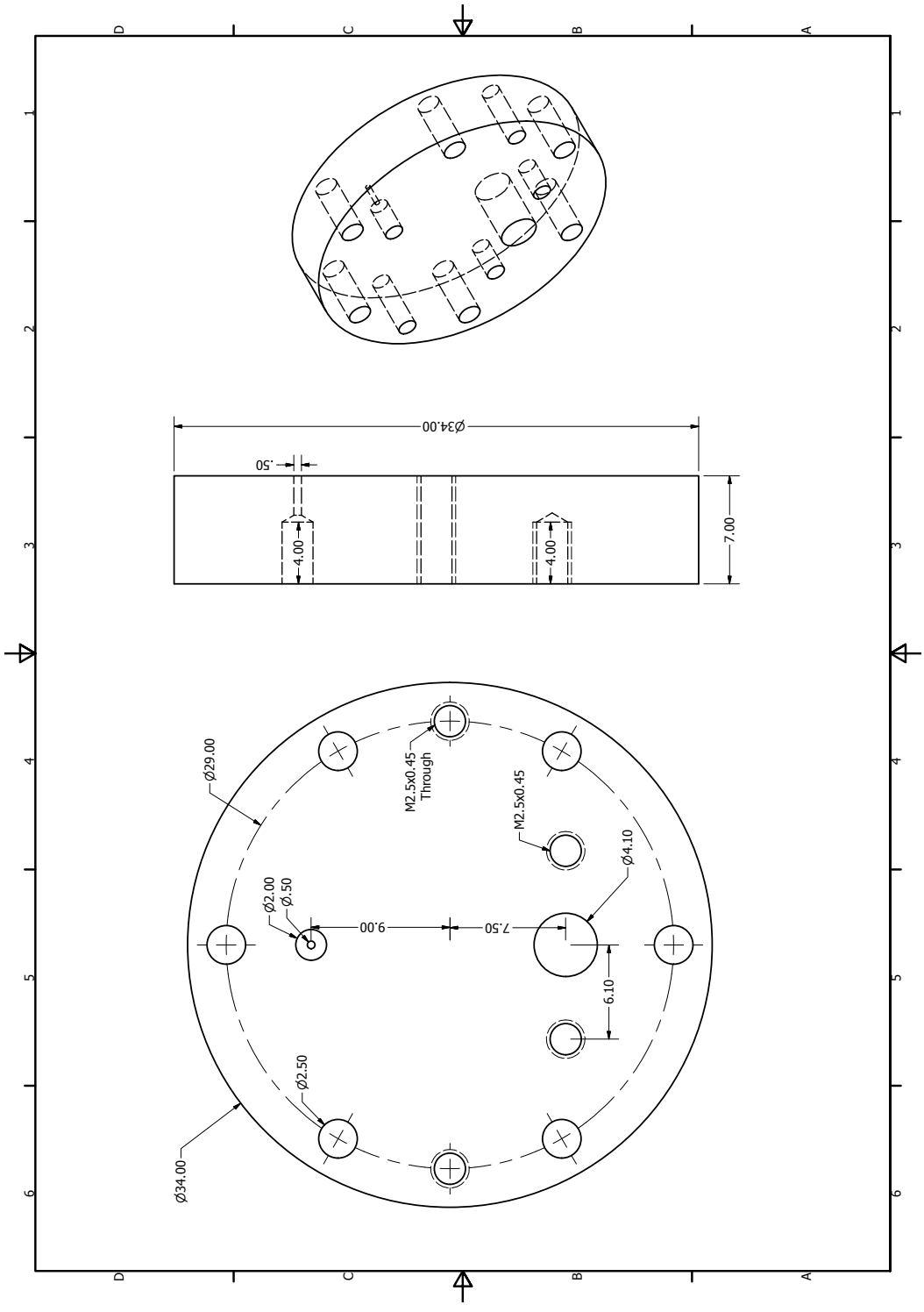

Figure B.1: Top of Optimal Parameter Re-entrant Cavity.

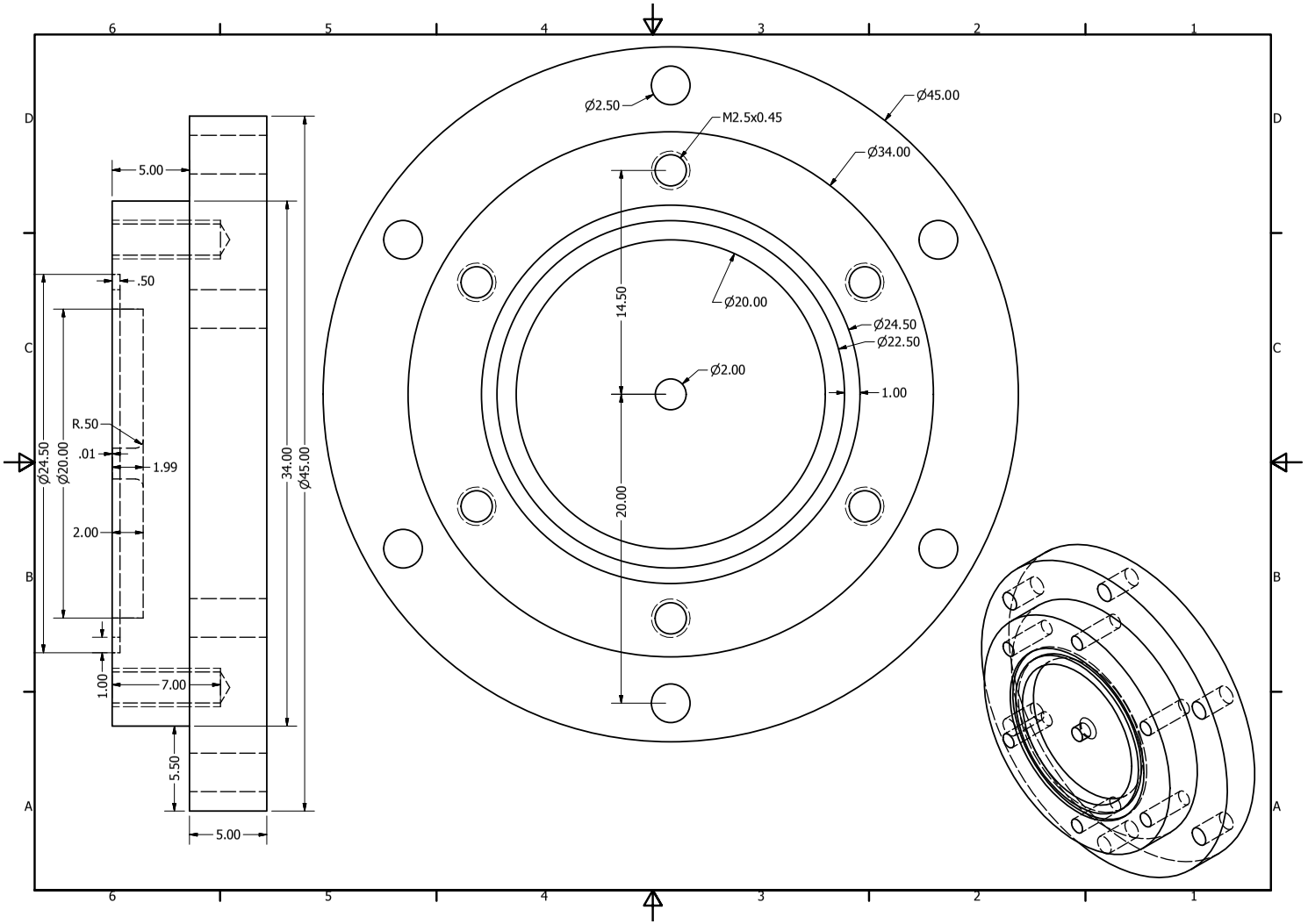

Figure B.2: Bottom of Optimal Parameter Re-entrant Cavity.

B.3 Safe Re-entrant Cavity Drawing

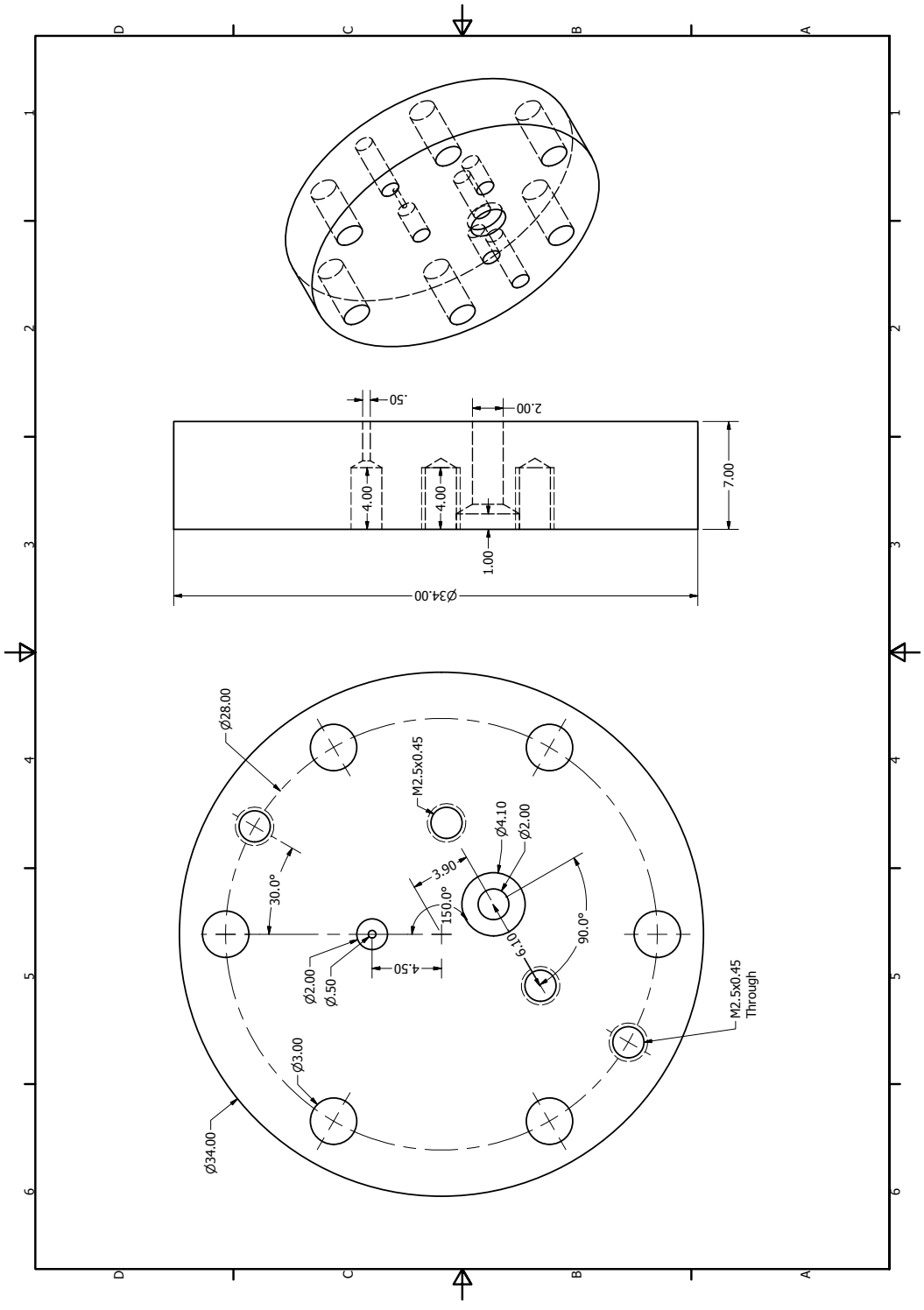

Figure B.3: Top of Safe Parameter Re-entrant Cavity.

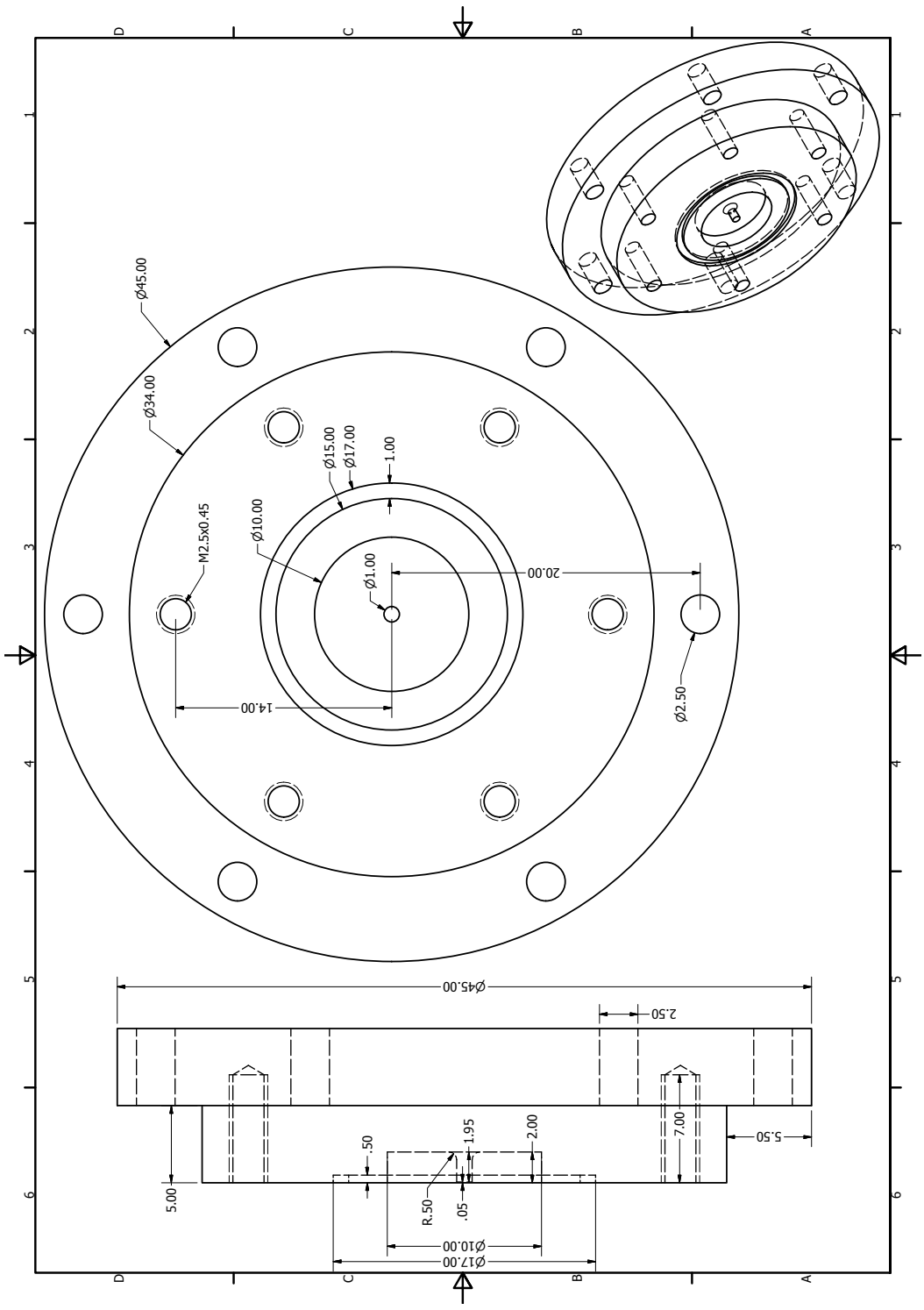

Figure B.4: Bottom of Safe Parameter Re-entrant Cavity.